Age and Hafnium Isotope Evolution of Sudanese Butana and Chad Illuminates the Stenian to Ediacaran Evolution of the Southeast Saharan Metacraton

Morgan L. Blades[1], Alan S. Collins[1,*], John Foden[1], Justin L. Payne[2], Kurt Stüwe[3], Mahmoud Hassan[4], Tamer Abu-Alam[5]

[1] *Tectonics and Earth Systems Group (TES), Department of Earth Sciences, The University of Adelaide, Adelaide, SA 5005, Australia.*

[2]*School of Built and Natural Environments, University of South Australia, Adelaide, Australia*

[3]*Institut für Geologie und Paläontologie, University of Graz, A-8010 Graz, Austria*

[4] *Geology Department, Faculty of Science, Suez Canal University, 41522 Ismailia, Egypt*

[5]*Universitetsbiblioteket, Norges arktiske universitet, 9037 Tromsø, Norway*

* Corresponding author at alan.collins@adelaide.edu.au

ABSTRACT

The Saharan Metacraton is a poorly known tract of pre-Neoproterozoic continental crust that occupies the area between the juvenile Arabian Nubian Shield, in the east, and the Tuareg Shield to the west. Neoproterozoic orogenesis (i.e. Dahomeyide, Oubanguides and East African orogenies) affect the west, the south and the east of the metacraton; respectively, which led to deformation, emplacement of igneous bodies, and localised episodes of rift-related magamatism. Details about interior regions of the Saharan Metacraton are poorly known, with much of it covered by Phanerozoic cover. The basement outcrops in Sudan, Chad and Libya have been the subject of few modern geochronological studies. Here we present results from the first zircon geochronology and *in-situ* zircon hafnium isotope investigations from both the Sudanese Butana and central Chad. The terranes in Butana, formed to the east of pre-Neoproterozoic continental crust of the Saharan Metacraton, with the oldest juvenile magmatism ($\varepsilon_{Hf}(t)$ of +4.89 to +7.89) at ca. 839 Ma, followed by subsequent magmatism at ca. 787 Ma. The ca. 787 Ma event (seen elsewhere in the East African Orogen) is interpreted to represent volcanic-arc collision and accretion with the kernel of the Saharan Metacraton. The ca. 839 Ma magmatism is contemporaneous with the accretion of the Tonian (ca. 850 Ma) arc terranes of the Arabian Nubian Shield and marks subduction to the east of the Saharan Metacraton. The magmatic history of the Ouaddaï region in Chad begins in the late Mesoproterozoic, with localised rifting, resulting in the emplacement of juvenile granites (ca. 1030 Ma). The Cryogenian and Ediacaran in the Saharan

Metacraton reveal a complicated history of magmatism and deformation. Age data from Chad show the emplacement of granites (from melting of Mesoproterozoic crust: $\varepsilon_{Hf}(t)$ = +2.04 and -4.07) at ca. 665–654 Ma, coeval with the main East African Orogeny and accretion of the other ANS terranes to the Saharan Metacraton at ca. 650–580 Ma. The youngest tectonothermal event within the Saharan Metacraton is recorded by emplacement of granites between 580–550 Ma ($\varepsilon_{Hf}(t)$ values of -17 to -31) in southern Chad.

KEYWORDS
Butana, Chad, Saharan Metacraton, U–Pb Geochronology, zircon, hafnium

INTRODUCTION:

The basement of northern central Africa is one of the most poorly known geological regions on the planet. The ~500,000 km^2 area is largely covered by the Saharan Desert and older Phanerozoic sedimentary rocks. However, even where rocks crop out, little modern research has been undertaken due to their remoteness and difficulty of access in Algeria, Libya, Chad and Sudan. Conflicting geological, geochronological and isotopic observations have led to the region being referred to by many names; the Nile Craton (Kennedy, 1964) Sahara-Congo Craton (Kroner, 1977), Eastern Saharan Craton, or Central Saharan Ghost Craton (Black and Liegeois, 1993). Abdelsalam et al. (2002) coined the name 'Saharan Metacraton' to best represent this enigmatic block, which remained a coherent rheological entity during the Neoproterozoic, rather than fully tectonically mobile, as seen in the Arabian Nubian Shield to the east. The Neoproterozoic destabilisation of the region was first recognised by Kennedy (1964) who initially introduced the term Pan-African tectonothermal event. However, he was unable to distinguish the area from other Neoproterozoic orogenic belts. The Saharan Metacraton (Fig 1a) is bounded to the east, west, and south by lithospheric-scale suture zones resulting from collisional events during the Neoproterozoic and has been treated as a coherent continental block in many Neoproterozoic reconstructions (e.g. Collins and Pisarevsky, 2005; Li et al., 2008; Merdith et al., 2017; Merdith et al., 2020; Pisarevsky et al., 2008). Recently, Şengör et al. (2020) suggested that instead of being a coherent block, that the region represents a large Neoproterozoic accretionary complex extending through from the West African Craton to the Arabian Nubian Shield.

To examine the nature of this extensive enigmatic region, we here provide some of the first U–Pb data and the only *in-situ* zircon Hf isotope data for the central and the eastern parts of the Saharan Metacraton (i.e., the central and southern parts of Chad and Butana in Sudan). These provide a window into the timing and nature of Mesoproterozoic and Neoproterozoic magmatism within the central regions of the Saharan Metacraton, as well as helping to further elucidate the relationship between the Saharan Metacraton and the Arabian Nubian Shield as Gondwana coalesced.

REGIONAL GEOLOGY
Saharan Metacraton

The Saharan Metacraton refers to pre-Neoproterozoic continental crust that occupies the north–central parts of Africa and extends to the Sahara Desert and Sahel (Fig. 1a). This tract of continental crust extends from the Arabian Nubian Shield in the east to the Tuareg Shield in the west (Abdelsalam et al., 2002). Abdelsalam et al. (2011) demonstrated that high S-wave velocity anomalies exist in the upper 100 km beneath the region, which is typical of cratonic lithosphere. However, by 175–250 km the anomaly is depressed that may represent the loss of its cratonic root, presumably during the Proterozoic. Recent geophysical data (Sobh et al., 2020) show the existence of three cratonic remnants (Murzuq, Al-Kufrah, and Chad) within the metacraton. These cratonic remnants are underlain by a thicker lithosphere compared to the rest of the metacraton (Fig. 1a). Neoproterozoic deformation, metamorphism, and magmatism seen through much of the Saharan Metacraton reflect its remobilisation and partial destabilisation as a result of collisional related deformation (Abdelsalam et al., 2011). The thin lithosphere (e.g. Sobh et al., 2020) was used to an extreme by De Wit and Linol (2015), who suggested that the whole region was simply floored with Neoproterozoic crust, which is supported by the new reconstruction of Şengör et al. (2020). Existing sparse geochronologic and isotopic data (e.g., Zhang et al., 2019; Bea et al., 2011; Shnellnutt et al., 2019, 2017; Evuk et al., 2014; Küster et al., 2008) indicate, however, that the crust is heterogeneous (Abdelsalam et al., 2011) and contrasts with the Neoproterozoic juvenile crust of the Arabian Nubian Shield to the east and the Archaean continental crust of the Congo Craton in the south (de Wit and Linol, 2015). The Saharan Metacraton is dominated by medium- to high-grade gneisses, metasedimentary rocks, migmatites, with

lesser occurrences of granulites and low-grade volcano-sedimentary rocks. These Precambrian rocks are exposed as uplifted massifs within Cretaceous and younger cover rocks (Abdelsalam et al., 2002; Küster et al., 2008). There are two dominant structural trends within the Saharan Metacraton; an ENE–WSW trend, and a younger N–S trend. The former has been documented in the Bayuda Desert, Nubian Desert, Kordofan and Darfur, Uweinat and Jebel El Asr inlier and has been referred to as the Zalingei folded zone (Abdelsalam et al., 2003; Abdelsalam et al., 2002; Abdelsalam and Stern, 1996; Schandelmeier et al., 1987; Schandelmeier et al., 1994; Stern, 1994; Sultan et al., 1994; Toteu et al., 1987; Toteu et al., 1994; Vail, 1983). North–south trending structures occur in the north–east and are parallel to the Keraf-Kabus-Sekerr shear zone (Küster and Liégeois, 2001; Abdelsalam and Dawoud, 1991; Stern, 1994; Abdelsalam and Stern, 1996). This is interpreted to be the result of an arc-continental collision that brought together the Saharan Metacraton with the Arabian Nubian Shield at around 714-645 Ma. (e.g. Evuk et al., 2014; Abu-Alam et al., 2014). Itself representing the northern extension of the East African Orogen (Abdelsalam et al., 2003; Abdelsalam et al., 2002; Abdelsalam and Stern, 1996; Küster and Liégeois, 2001).

Geochronologic and isotopic data from the Saharan Metacraton are highly variable, with ages ranging from ca. 3100–500 Ma. Archaean–Palaeoproterozoic ages within the metacraton have been reported for gneissic and granulitic rocks, using Rb–Sr and U–Pb zircon geochronology (Pin and Poidevin, 1987; Stern, 1994; Sultan et al., 1994; Zhang et al., 2019; Bea et al., 2011). Work, reported by de Wit and Linol (2015), has suggested that the southern parts of the metacraton are composed of mainly late Mesoproterozoic crust. However, Shellnutt et al. (2017, 2019) interpreted the volcanic-arc signature of 590 Ma granitic rocks from southern Chad (i.e., southern parts of the metacraton) to be formed due to a subduction process. In the east of the metacraton, existing geochronology (U–Pb, Rb–Sr) suggests ages between 2629–1922 Ma (Liégeois et al., 1994; Stern, 1994; Sultan et al., 1994). These are intruded by early Neoproterozoic–late Mesoproterozoic granites (ca. 1100–900 Ma – e.g., Evuk et al., 2014; Küster et al., 2008), which were deformed during the Neoproterozoic. Post-collisional 600–560 Ma granites are abundant throughout the north-eastern Saharan Metacraton, with the exception of the Uweynat massif (Bea et al., 2011; Abdelsalam et al., 2002; Küster and Harms, 1998; Stern, 1994).

Within the centre of the Saharan Metacraton, there are four distinct Precambrian massifs that outcrop in Chad, Libya and Sudan (Fig. 1a); the Tibesti, the Ouaddaï, the Guera (Central Massif)and the Mayo Kebbi massifs (Abdelsalam et al., 2002, Kusnir and Moutaye, 1997, Schluter, 2008). These outcrops form much of the exposed Saharan Metacraton, yet there has been little geological work done in the area.

Central Massif

The Central Massif (Guera), located in the centre of Lake Chad Basin, encompasses three main massifs––Abou Telfan, Kengas and Melfi, as well as numerous isolated outcrops and inselbergs (Fig. 1b). Lithologically, the Central Massif is composed of Neoproterozoic metavolcanic (amphibolite, meta-andesite), metamorphic rocks (schists, marbles, quartzite, paragneiss and orthogneiss; Isseini et al., 2013; Kusnir and Moutaye, 1997) intruded by 595 and 545 Ma granitoids and gabbros (Shellnutt et al., 2020, 2019, 2018, 2017; Nkouandou et al., 2017; Couzinié et al., 2020). Petrographically, the granitoids are classified into alkaline granites, monzonites and syenites. At the periphery, the outcrop disappears under the formations of the Lake Chad Basin (Schneider and Wolf, 1992). The studied samples (Fig. 1b) are from the granitoids (sample CM1 and CM2) and the metamorphic rocks (i.e., garnet-bearing gneisses - sample CM3).

Ouaddaï region

The Ouaddaï region is located to the north-east of the Central Massif (Fig. 1b) and represents the easternmost exposure of the Pan-African Central Africa Orogenic Belt (Bessoles and Trompette, 1980; Toteu et al., 2004; Djerossem et al., 2020). The northern part of the Ouaddaï region is made of granitoïds and migmatites that have been extensively eroded. Volcanosedimentary rocks form local septa between granitoids and are known as Goz Beida Group. The Goz Beida Group is composed of a series of quartzites, schists and amphibolites. The granitoids are made up of two distinct intrusive series: 1) calc-alkaline rocks consisting of two mica-bearing porphyritic and pegmatitic granites. 2) Alkaline rocks composed of biotite-bearing granites, syenites, monzo-gabbros and gabbros. Both of these suites are associated with network of fine-grained granites, diorites, pegmatites and northeast –

southwest trending veins (Schneider and Wolf, 1992). Sample OU2 was collected from coarse-grained monzogranite from the northern part of the Ouaddaï region.

On the other hand, the southern Ouaddaï region is dominated by low-grade metamorphic rocks (Lele Series). The Lele Series is composed of intensely deformed metasediments of muscovite-biotite, muscovite-bearing quartzite and metapelites that intercalated by marbles and calc-silicate gneisses. Rare amphibolite bands were observed alternating with the metasediments. Greenschist facies mineral assemblages are observed in the metasediments, but rare garnet and sillimanite are noted. The main structural foliation in the metasediments strikes NE-SW and is associated with isoclinal folds. The isoclinal folds are refolded during a later deformation event around vertical axial planes subparallel to the main foliation forming open vertical folds. Djerossem (2018) suggested a maximum depositional age of these metasediments at 1 Ga based on U-Pb dating of detrital zircons. Pre- and syn-tectonic batholiths of muscovite and biotite leucogranites are observed wrapped into the main foliation. Post-tectonic smaller intrusions of monzonite, granodiorite and granite are observed cutting across the foliation. The pre- and syn-tectonic granites formed from tholeiitic and peraluminous magmas at ca. 750 Ma to 600 Ma, while the post-tectonic granites formed at ca. 590–540 Ma and have high-K calc-alkaline to shoshonitic chemical signature (Toteu et al., 2004; Shellnutt et al., 2019; Djerossem et al., 2020). Samples OU3, 4 and 5 were collected from the metasediments while sample OU1 was collected from the syn-tectonic monzogranite.

Mayo Kebbi region

The Precambrian basement exposed in the Mayo-Kebbi massif in southwestern Chad is part of the Pan-African Central Africa Orogenic Belt (Bessoles and Trompette 1980; Black and Liégeois 1993; Abdelsalametal. 2002; Liégeois et al. 2013). Most of the basement is covered by Phanerozoic platform sedimentary rocks. The basement of Mayo-Kebbi massif is composed of metavolcanic–metasedimentary sequences intruded by granites (Kasser 1995; Doumnang 2006; Penayeet al. 2006; Isseini 2011; Pouclet et al. 2006; Isseini et al., 2012; Vanderhaeghe et al. 2020). The metavolcanic–metasedimentary sequences trend NNE-SSW and are composed of two series; the Zalbi series to the

west and the Goueygoudoum series to the east. The Goueygoudoum series includes metabasalt, metacarbonatite and metacherts (Kasser 1995; Doumnang 2006; Pouclet et al. 2006; Isseini 2011), while the Zalbi series is composed of metagabbro, metabasalt, schist and serpentinite. The metamorphic grade increase from greenschist facies in the Goueygoudoum series to the amphibolite facies in the Zalbi series.

The metavolcanic–metasedimentary sequences are intruded by the Mayo Kebbi batholith at ca. 737–638 Ma (Penaye et al., 2004; 2006; Schneider and Wolf, 1992; Vanderhaeghe et al. 2020; Isseini 2011). The Mayo Kebbi batholith is made of a calc-alkaline magmatic suite (e.g., diorite, tonalite and granodiorite; Wacrenier 1962; Kasser 1998; Doumnang 2006; Penaye et al. 2006; Pouclet et al. 2006). The metavolcanic–metasedimentary sequences and the Mayo Kebbi batholith are intruded by post-tectonic granitoids (Zabili granite, monzodiorite and porphyritic granite) at ca 570 Ma (Kasser1995; Penaye et al., 2006; Schneider and Wolf, 1992; Shellnutt et al., 2017; Shellnutt et al., 2018; Isseini et al 2012). The studied samples MK1 and 2 are from a mylonitised granite and monzogranite; respectively.

Tibesti region

Although no samples were collected in the current study from the Tibesti region, the geology of Tibesti is presented here to have a regional overview of the Saharan Metacraton. The Precambrian exposures in the Tibesti are comprised of two distinct assemblages separated by an angular unconformity (e.g. Ghienne et al., 2012 and references therein). The lower assemblage (in the north east) is made up of amphibolites, pyroxenites, quartzites, marbles, gneiss and mica-schists. Within the upper assemblages, there are a series of metasedimentary units interlayered with metavolcanic rocks. These are cross-cut by the Super Tibestian magmatic series (e.g., El Makkrouf, 1988) and the Ben Ghnema batholith (600–550 Ma, Ghuma and Rogers, 1978; Suayah et al., 2006), interpreted to be related to result from westward subduction beneath the eastern margin of the basement of the Murzuk Basin (El Makkrouf, 1988; Ghuma and Rogers, 1978; Suayah et al., 2006). Post tectonic granites suggest deformation ended sometime before ca. 558 Ma (Suayah et al., 2006).

Terranes surrounding the Saharan Metacraton

The Saharn Metacraton is surrounded by the Arabian Nubian Shield from the east, Oubanguides belt from the south and Tuareg Shield from the west. Although samples studied in the current contribution are not from Oubanguides nor Tuareg Shield, we present a summary of the geology of these two belt/shield in order to understand the regional geology.

Arabian Nubian Shield

The Arabian Nubian Shield lies to the east of the Saharan Metacraton. The shield represents the northern expression of the East African Orogen (Stern, 1994) and is characterised by Neoproterozoic juvenile crust that formed as a series of volcanic arcs (Abu-Alam et al., 2014; Johnson et al., 2011; Johnson and Woldehaimanot, 2003; Stern, 2002). The shield is dominated by low-grade volcano-sedimentary rocks in association with plutons and ophiolitic remnants (Abdelsalam and Stern, 1996; Abu-Alam and Hamdy, 2014; Blades et al., 2019; Blades et al., 2015; Cox et al., 2012; Kröner et al., 1991; Robinson et al., 2014; Shackleton, 1996; Stern, 1994). Medium- to high-grade metamorphic rocks are found as core complexes (Abu-Alam and Stüwe, 2009, Abu-Alam et al., 2014).

Widespread acceptance of the juvenile character of most of the Arabian Nubian Shield has come about in the past decade, although consensus is not universal (Johnson, 2014). The Bayuda Desert has been interpreted to represent the eastern margin of the Saharan Metacraton (i.e., Keraf Suture) and is characterised by juvenile rocks (Küster and Liégeois, 2001; Evuk et al., 2014; Küster et al., 2008). Some granitoids show TDM model ages of c. 900-910 and are interpreted to be formed during 920–900 Ma Bayudian orogenic event (Küster et al 2008). ^{40}Ar–^{39}Ar dating on biotite and hornblende, from deformed granites in Bayuda suggest that the transgressive deformation along the Keraf suture due to the closing of the Mozambique Ocean (Abdelsalam et al., 1998; Küster and Liégeois, 2001) ended by ca. 580 Ma (Küster and Liégeois, 2001).

The juvenile character of the Arabian Nubian Shield is observed from other terranes (e.g., northeast Sudan, Eritrea, Ethiopia, Egyptian Eastern Desert, Sinai and Saudi Arabia). Some of the closest exposures to Bayuda are in the Western Ethiopian terrane where the oldest rocks in the area formed in an intra-oceanic setting and date back to ca. 855 Ma and there is no evidence of pre-Neoproterozoic crust

(Blades et al., 2015). Magmatism and deformation are seen at 810–770 Ma, 660–655 Ma and ca. 584 Ma (Blades et al., 2015). All the rocks in the Western Ethiopian terrane have juvenile $\varepsilon_{Hf}(t)$ values of +4.5 to +10, suggesting that the influence of continental crust was minimal.

Further north, in Eritrea, juvenile arc magmatism occurred between ca. 850–740 Ma (Andersson et al., 2006; Teklay et al., 2003), followed by intrusion of post-tectonic granites at 640–600 Ma (Avigad et al., 2007) and amphibolite-facies metamorphism at ca. 590 Ma due to final continental collision in the area (Andersson et al., 2006). The Precambrian rocks of the Egyptian Eastern Desert have been suggested to represent six main pulses of magmatism at 1) 705–680 Ma, 2) ca. 654 Ma, 3) ca. 630 Ma, 4) 610–604 Ma, 5) 600–590, and lastly 6) ca. 540 Ma (Andresen et al., 2010; Augland et al., 2012; Lundmark et al., 2012; Shalaby et al., 2005; Stern and Hedge, 1985). Hafnium and oxygen isotopes in the North Eastern Desert show $\delta^{18}O$ values (+5.15 to +6.70) and $\varepsilon_{Hf}(t)$ values (+6.3 to +10.6), which were interpreted to reflect melting of a juvenile Neoproterozoic mantle source that assimilated slightly older Neoproterozoic crustal material (Ali et al., 2016). The northernmost extent of the Arabian Nubian Shield is defined by the Sa'al metamorphic complex in Sinai (Hassan et al., 2014) which has Mesoproterozoic age (ca. 1100–1000 Ma) and intruded by post-collisional calc-alkaline (ca. 635–590 Ma) and alkaline (ca. 600–580 Ma) granitic plutons (Be'eri-Shlevin et al., 2012; Johnson, 2014). The rocks in Sinai have average $\delta^{18}O$ values of 5.7 to 5.8‰ indicating the dominance of mantle-like $\delta^{18}O$ sources with higher values in north-western Sinai (6.9-8.2‰). Hafnium isotopes, complement oxygen isotopes, revealing a gradual transition from lower $\varepsilon_{Hf}(t)$ values in the north-western regions (+5.5 to +5.9) to slightly higher in south-eastern region (+9.2 to +13.9) (Be'eri-Shlevin et al., 2012).

Butana

The Butana region is a part of the Arabian Nubian Shield and lies between the Bayuda Desert and the Western Ethiopian terrane (250 km southeast of Khartoum). Butana is one of the few exposures of Precambrian basement in Central Sudan (Fig. 1c) and is thought to be located close to the transition between the juvenile Arabian Nubian Shield and the enigmatic Saharan Metacraton. Little geological

work has been done in the region, therefore samples collected from this region provide valuable insight into the relationship between the Saharan Metacraton and the Arabian Nubian Shield. The region is characterised by flat-lying topography with isolated basement exposures. The area consists of low-grade metavolcanic rocks (arc assemblage), pre- and syn-tectonic granitic intrusions. In particular, the presence of serpentinites, ophiolitic metagabbro and high-grade metamorphic rocks may identify it as part of the Arabian-Nubian Shield.

The high-grade metamorphic rocks crop out at the NW (Reira area) and SE (J. Baashomiyat) ends of the mapped area (Fig. 1c). The metamorphic rocks show mineral assemblages of upper amphibolite facies and intruded by syn-tectonic granitics bodies. The contact between the metamorphic rocks at J. Baashomiyat and the serpentinites is a tectonic contact. While the contact between the metamorphic rocks at Reira area and the surrounded metavolcanics is covered by a thick soil cover. Lenses and bands of marble trending NE-SW are intercalated with the metavolcanics. Post-tectonic intrusions (i.e., granites and gabbros) intruded both the serpentinites and the metavolcanics. Samples presented here were collected from the metamorphic rocks at Reira area (BU3 - meta porphyritic andesite), small granites body intruded the Reira area (BU1 - monzogranite). Samples BU4 and 5 were collected from the metamorphic rocks (paragneiss) at J. Baashomiyat while samples BU2 and BU6 represent the granitic intrusion (syenogranite) from the center part of the mapped area.

The main metamorphic foliation trend in the low-grade rocks (serpentinites and metavolcanics) is northeast-southwest (Fig. 1c) with steep foliation plains and sub-horizontal lineation. At J. Baashomiyat, right-lateral shear sense indicators are observed. In the high-grade rocks, at least three deformation phases were observed in the field. D1 associates with northeast-southwest foliation planes and D2 associates with high-temperature folding mechanism which gave the high-grade rocks domal pattern. While D3 is a faulting phase with brittle features. The peak metamorphism most probably occurred after the D2 as indicated by the migmatic features.

Oubanguides

The Oubanguides sits at the southern extent of the Saharan Metacraton and broadly consist of Paleoproterozoic basement thrusted over the Congo Craton, with granulite facies metamorphism following collision (Toteu et al., 2004). The region is divided into three tectonic units separated by shear zones. These are, from south to north, the schistose and gneissic Yaoundé domain, consisting of extensive nappes thrust over the Congo Craton (Owona et al., 2011); the reworked Paleoproterozoic Adamawa-Yadé domain (Tchakounté et al., 2017), intruded by numerous syn- to late- tectonic ca. 630–570 Ma granitoids; and, Western Cameroon domain (volcano-sedimentary schistose and gneissic rocks), which was intruded by calc-alkaline granites (Itiga et al., 2019) between 660–580 Ma (Toteu et al., 2001). The oldest intrusions are metagabbro rocks in the northern Yaoundé domain that are dated at 660 ± 22 Ma. These are thought to have intruded during upper-plate extension in response to subduction further south, facilitating deposition within the Yaoundé Basin (Toteu et al., 2006). Deformation and metamorphism are constrained to ca. 660–600 Ma (Nkoumbou et al., 2014; Owona et al., 2011; Toteu et al., 2006).

Tuareg Shield

The Tuareg Shield (to the west of Saharan Metacraton) is composed of 25 terranes (Liégeois, 2019) that are Archaean to Neoproterozoic in age, juxtaposed by large displacements along mega-shear zones (Black et al., 1994; Liégeois et al., 1994). Most of these shear zones are N–S oriented and are associated with granitoids of several ages at 800–820 Ma, 730 Ma, 620–580 Ma and 575–545 Ma (Caby, 1987; Fezaa et al., 2010; Liégeois et al., 2005; Liégeois et al., 1994; Liegeois et al., 2003). Raghane shear zone is one of these zones and is interpreted to represent the western boundary of the Saharan Metacraton, which was tectonically active from ca. 730–580 Ma (Henry et al., 2009; Liégeois et al., 1994). The Raghane shear zone separates the Tuareg Shield into two parts (Black et al., 1994), where the eastern part belongs to Saharan Metacraton and includes four terranes (Djanet, Edembo, Aouzengueur and Barghot). These terranes were juxtaposed prior to 700 Ma (Liégeois et al., 1994; Fezaa et al 2010). While the western part (e.g. Assodé-Issalane terrane) is affected by early tectonism due to collision with the Saharan Metacraton between 700–670 Ma.

The central part of the shield (Central Hoggar) preserves amphibolite- to granulite-facies Archaean and Paleoproterozoic terranes, with evidence of Neoproterozoic reworking (Bendaoud et al., 2008; Liégeois et al., 2003; Peucat et al., 2003). The stabilisation of the Hoggar region (sometimes known as LATEA; e.g., Liégeois et al., 2003), is marked by the formation of mega-shear zones and the intrusion of granitoids batholiths (Acef et al., 2003) accompanied by high-temperature metamorphism (Bendaoud et al., 2008). These tectono-thermal events are focussed at 620–600 Ma (Acef et al., 2003; Bendaoud et al., 2008) and ended by ca. 572 Ma, when post-tectonic plutons intruded (e.g. the Temaguessine pluton, Abdallah et al., 2007). Later alkali magmatism occurs at ca. 524 Ma (e.g. the Tioueine pluton, Azzouni-Sekkal et al., 2003; Paquette et al., 1998).

Petrography
High-grade gneisses and granitoids

Butana

Sample BU1 - monzogranite

This sample is composed mainly of coarse- to medium-grained microclinized K-feldspar, quartz and plagioclase. Anhedral quartz grains are usually deformed with wavy to undulatory extinction. Oxide, epidote, zircon are the main accessories. It exhibits a faint gneissic appearance of slightly decomposed biotite to oxide and chlorite.

Samples BU2 and BU6 - syenogranite

The syenogranites are composed mainly of megacryst of microclinized perthitic K-feldspar, inclosing fine plagioclase characterized by albite rims, in a medium-grained groundmass of quartz and plagioclase. Biotite is fresh in general, but occasionally is slightly altered, where zircon and apatite are the abundant accessory minerals.

Ouaddaï region

Samples OU1 and 2 - coarse-grained syenogranite

Both samples are coarse-grained syenogranite and composed of quartz + microclinized K-feldspar + plagioclase + biotite (15 – 17 %). Sphene, zircon, apatite and oxides are accessories. Sample OU1 is characterized by deformation and slight mylonitization observed as preferred orientation of biotite and surrounding quartz. OU2 is characterized by porphyritic texture of microclinized perthitic orthoclase mega phenocrysts. Microcline exhibits patch shape. Very coarse- to medium-grained anhedral quartz are deformed and showing wavey to undulose extinction. Coarse-grained fresh plagioclase has simple and lamellar twinning, while fine inclusions of plagioclase are characterized by albite rims within the microclinized perthitic K-feldspar. Silica liberation as myrmekitic texture in plagioclase is observed but contains inclusions of biotite and Opaque.

Sample OU3 – orthogneiss

Oxide- rich orthogneiss is a coarse-grained banded rock of alternating quartz and muscovite bands; well foliated muscovite bands incorporate minor chlorite and plenty of opaque minerals. Quartz-plagioclase bands are poor or have no opaques, but quartz usually exhibits uneven extinction. Epidote is found as an accessory mineral. Muscovite flacks are up to 0.7 mm in length and opaques are up to 1 mm in diameter.

Central Massif and Mayo Kebbi samples

Sample CM1 – Monzogranite (Central Massif)

Monzogranites crop out in the Central Massif are coarse to medium-grained rock and are composed mainly of quartz, perthitic microclinized K-feldspar, plagioclase and more than 5 % chloritized biotite. Coarse-grained perthitic orthoclase is partial to mainly microclinized accompanied with medium- to occasionally coarse-grained plagioclase. Interstitial deformed medium-grained quartz displays uneven extinction, while the brittle deformed biotite is partly decomposed to chlorite and opaques with apatite inclusions.

Sample CM2 – Syenogranite (Central Massif)

The coarse-grained syenogranites in the Central Massif are composed mainly of perthitic K- feldspar megacrysts in medium-grained quartz and plagioclase. The perthitic K- feldspar encloses plagioclase grains that showing albite rims, while medium- to coarse-grained plagioclases show simple and lamellar twinning without zonation. Quartz can be found as very coarse-grained phenocrysts in addition to interstitial deformed medium-grain with uneven extinction. Highly chloritized-biotite represents about 10 % of the rock. Oxides are present as euhedral accessory minerals.

Other samples - Coarse-grained granite (Central Massif)

Other granitic samples which were not considered for geochronology are coarse-grained and composed mainly of microclinized perthitic K- feldspar in a medium-grained groundmass of quartz and plagioclase. Few euhedral medium- to coarse-grained crystals of plagioclase are observed and characterized by highly altered cores that obscure the twining. Fine inclusions of plagioclase are characterized by albite rims within the microclinized perthitic K-feldspar. The myrmekitic texture is widely observed and developed as silica liberation. Interstitial corroded medium-grained quartz exhibits uneven extinction. Mafic minerals occurred as biotite ± Hb, where biotite is partly decomposed to chlorite and opaques and exhibits twisted cleavages as brittle deformation. sphene, oxide, epidote present as accessories.

Mayo Kebbi region

Sample MK1 - mylonitised granite (Mayo Kebbi Region)

Mylonitized granite is composed of coarse-grained perthitic microclinized K-feldspar with few plagioclase grains in fine- to medium-grained mylonitized matrix. Quartz grains along mylonitization are recrystallized after deformation. Preferred oriented biotite liths follow the mylonitization with minor fine-grained hornblende. Zircon, apatite, sphene, oxide are accessories, while epidote is an alteration product.

Samples MK2 and MK3 – monzogranite (Mayo Kebbi Region)

Two monzogranite samples from Mayo Kebbi Region were examined geochronological. They are coarse-grained porphyritic granite and are composed of perthitic K-feldspar and quartz. Plagioclase phenocrysts occur in a medium-grained groundmass of K-feldspar, quartz and plagioclase. Very coarse-grained perthitic orthoclase is partial to mainly microclinized and comprises fine inclusion of plagioclase characterized by albite rims. Quartz is very coarse-grained, anhedral, deformed with wavy to undulatory extinction. Medium- and very coarse-grained plagioclase shows zoning illustrated by gradational alteration. Deformed grains show twisted or dislocated lamellar twinning. Biotites are slightly chloritized and show no preferred orientation but clustering with brittle deformation. Hornblende occurrence is inconsequential. Zircon, sphene, apatite, oxide, and epidote are accessories.

Metasedimentary Rocks

Butana

Sample BU3 - meta porphyritic andesite

Petrographically, the rocks consist mainly of alteration product of volcanic rocks showing porphyritic texture (meta porphyritic andesite). Considering that the meta-andesite rocks are highly altered, primary crystal shapes and texture are barely preserved to allow recognition of the original minerals. It is essentially composed of chlorite minerals indicating derivation from mafic content (pyroxene and amphibole) with epidote. Rare quartz fragments exhibit irregular shapes with completely sericitized feldspar.

Samples BU4 and BU5 - paragneiss

Well-defined gneissic foliation is easily seen in the hand specimens of these samples, whilst partial melting endorses upper amphibolite facies. Quartz, plagioclase, K-feldspar and biotite are the major constituents without any remarkable metamorphic minerals, but biotite forms a faint to moderate foliation by clustering without preferred orientation of every single grain.

Ouaddaï region

OU4 - chloritized mica phyllite schist

Biotite is the main constituent and quartz is dominant, in addition to occurrences of some feldspar, muscovite, and opaque minerals. Fine-grained biotite, partly chloritized, shows a well-developed foliation, while muscovite is bounded as spindle bands within the biotite bands. Crenulation foliation and kink folding illustrate shear fabric and deformed quartz extinction. Few thin quartz veinlets cross-cut the rock.

OU5 - muscovite schist

This rock shows weak to moderate foliation due to the fine to very fine lamination of variable grain size of quartz associated with Muscovite. The easily seen muscovite enriched lamination constrained along the shearing planes. Microfolding of muscovite lamination is easily seen.

Central Massif and Mayo Kebbi samples

Sample CM3 - garnet-bearing psammitic gneiss (Central Massif)

This rock is characterized by well-foliated muscovite and Hb with biotite and chlorite in addition to garnet, while quartz is the main constituent of the groundmass with minor plagioclase in addition to K-feldspar and opaque as accessories. Two sets of foliations are observed. The first set is marked by well-oriented amphibole and muscovite, while the second set of foliation is characterized by the presence of biotite in addition to the amphibole and muscovite. Post-deformation garnets are observed. For the most part, epidote has no preferred orientation; but some elongated epidote follows the orientation of the second set of foliation.

METHODOLOGY

U–Pb zircon geochronology

Samples from meta-igneous rocks were collected from different locations from both Chad and Sudan (see Figs. 1b and c). Geochemistry is not available for these rocks and therefore rock classifications are based on field and thin section observations (Fig. 2; Table 1).

Zircon U–Pb analyses were conducted on a New Wave 213 nm Nd-YAG laser coupled with the Agilent 7500cs Inductively Coupled Plasma Mass Spectrometer (LA-ICP-MS) at the University of Adelaide. The spot size used was 30μm. Isotopes ^{206}Pb, ^{207}Pb, ^{208}Pb, ^{235}U and ^{238}U were measured. It should be noted that ^{204}Pb was measured, but there is an isobaric interference from ^{204}Hg present in the gas supplies and therefore is only an estimate. GEMOC GJ-1 zircon together with TIMS normalising data ^{207}Pb/^{206}Pb=607.7 ± 4.3 Ma, ^{206}Pb/^{238}U=600.7 ± 1.1 Ma and ^{207}Pb/^{235}U=602.0 ± 1.0 Ma (Jackson et al., 2004) were used to correct for the U–Pb fractionation. The Plešovice zircon internal standard (ID TIMS ^{206}Pb/^{238}U age=337.13 ± 0.37 Ma) (Sláma et al., 2008), was used to assess accuracy before and during the analysis of the unknowns. Plešovice analyses yield a weighted-mean ^{206}Pb/^{238}U age of 335.3 ± 1.3 with an MSWD of 0.41 (n=80).

Data were collected over three analytical sessions, corrected and filtered in software package GLITTER version 3.0 (Van Achterbergh et al., 2001). Concordia diagrams and weighted averages were calculated using ISOPLOT 4.11 for Excel (Ludwig, 2008). Concordance is calculated using ([^{206}Pb/^{238}U]/[^{207}Pb/^{206}Pb]*100). As many of these analyses show small amounts of Pb-loss, the ^{207}Pb/^{206}Pb isotopic system is often relied upon. Variable concordance cut offs were explored and 10%

is considered the most appropriate, with a more concordant filter (i.e. 5%) showing no real benefit. Data that failed the filter were treated with caution and where these were within a few % were still deemed to be useful in assessing these samples, however were not included in the main age calculations. Analyses with higher ^{204}Pb counts per second (>100) were more closely examined . All age uncertainties are quoted at a 2σ level.

Zircon Lu–Hf Isotope analysis

Analytical methods for zircon Lu–Hf isotope analysis follow Payne et al. (2013). Analyses were undertaken using a New Wave UP-193 ArF excimer laser attached to a Thermo-Scientific Neptune Multi-Collector ICP-MS at the University of Adelaide. The bulk of analyses were carried out using a beam diameter of ~50 μm for large and a minimum of ~ 25 μm for smaller grains. Typical ablation times were 40–100 s using a 5 Hz repetition rate, a 4 ns pulse rate, and an intensity of ~6–8 J/cm^2. Zircons were ablated in a helium atmosphere and Ar was added downstream of the ablation cell, with the addition of N_2 to the Ar sample gas flow (upstream of mixing with He).

Reduction of zircon data were undertaken using a macro-driven Hf isotope data reduction Excel spreadsheet, HfTRAX (Payne et al., 2013). The data were normalised to ^{179}Hf/^{177}Hf = 0.7325, using an exponential correction for mass bias. Ytterbium and Lu isobaric interferences on ^{176}Hf were corrected following the methods of (Woodhead et al., 2004).

The accuracy of the Yb and Lu corrections has been demonstrated by repeated analysis of standard zircons with a range in ^{176}Yb/^{177}Hf and ^{176}Lu/^{177}Hf values (Griffin et al., 2006). Before and during the analysis of unknowns, standards were analysed to check instrument performance and stability. The internal zircon standard used was Plešovice, which yielded a mean ^{176}Hf/^{177}Hf ratio of 0.282473 ± 0.00002. This compares to the published value of 0.282482 ± 0.000013 (2SD) by Sláma et al. (2008). Values for $\varepsilon_{Hf}(t)$, and $T_{DM}c$ were calculated using ^{176}Lu decay constant after Scherer et al. (2001). T_{DM} crustal was calculated using the methods of Griffin et al. (2002) with an average crustal composition of ^{176}Lu/^{177}Hf = 0.015. Lu–Hf data are presented in a $\varepsilon_{Hf}(t)$ v. preferred age plot (Fig.7). Uncertainties on Lu–Hf are quoted at the 2σ level. For igneous samples a single preferred crystallisation age was

adopted, though individual ages are quoted in Supplementary Table 2. In metasedimentary samples, individual grain ages are used.

RESULTS

All petrology (Fig. 2) and sample descriptions are located in Table 1 and analytical data are presented in the supplementary material. Description of CL characteristics for igneous samples are summarised in Table 1 and representative images are available in Figs. 3 and 4. Igneous U–Pb data are plotted on weighted average age plots and on Wetherill plots (Fig. 5a and b; $^{207}Pb/^{206}Pb$ v. $^{238}U/^{206}Pb$). Metasedimentary U–Pb data are represented on Wetherill plots and respective kernel density estimate plots (KDE; Fig. 6). Metasedimentary Lu–Hf data are presented in Figure 8 and data is available in Supplementary Table 2.

Zircon U–Pb geochronology—Gneisses and Granitoids
Butana
BU1 monzogranite (15°23'N 34°41'E)

Sixty-seven zircons were analysed targeting both rims and cores and of these forty-six were ≤ 10% discordant showing a range of $^{206}Pb/^{238}U$ ages between 867–738 Ma (Figs. 3 and 5a). Of these, eight grains were selected for Lu–Hf isotope analysis. Th/U ratios range from 0.73–0.35 in all but one analysis. This one zircon (BU1_09) also yielded the youngest age with a $^{206}Pb/^{238}U$ age of 738 ± 17 Ma and this age may be recording metamorphism of this sample. Of the remaining analyses, two yielded $^{206}Pb/^{238}U$ ages (ca. 765 Ma) significantly younger than the other near concordant analyses (Fig. 5a). These analyses were from CL-defined rims, but their $^{207}Pb/^{206}Pb$ ages are in the range of the other near concordant analyses, suggesting that they have lost an amount of radiogenic Pb. Excepting these analyses, the ≤ 10% discordant analyses yield $^{206}Pb/^{238}U$ ages between 867–797 Ma (Th/U = 0.34–0.75; n=43) with a weighted average of 827 ± 5 Ma (n = 43, MSWD = 1.9; Fig. 5a; Supplementary Table 1). The $^{177}Hf/^{176}Hf$ ratios of these grains vary between 0.282516 and 0.282475 (Supplementary Table 2 and Supplementary Fig. 1). The overlapping initial Hf isotope ratios and lack of differentiating zircon characteristics, suggest that these zircons may have lost some Pb post-formation, and the above quoted age likely represents a younger estimate of the true age. Because of this, the $^{207}Pb/^{206}Pb$ weighted

average age 855 ± 11 Ma (MSWD = 0.6, n = 43) is interpreted as a more accurate representation of the age of crystallisation of the protolith. A slightly more precise estimate is provided by using the ^{206}Pb/^{238}U weighted average of only the oldest twenty-two (of the 43) analyses. This yields an age of 839 ± 5 Ma (MSWD=0.55) that we interpret as the best estimate for the age of crystallisation of the protolith of this gneiss. The single zircon that yielded a ^{206}Pb/^{238}U age of 738 ± 17 Ma may represent the age of metamorphism of this sample, although being only one analysis, this must be treated with caution.

Hafnium isotope analyses give ε_{Hf}(t) values between +6.59 to +9.54. This suggests juvenile sources, with minimal continental crust involvement (Fig. 7a).

BU4 + BU5 Paragneiss (14°37'N 34°56'E and 14°38'N 34°56'E)

Of the fifty-two analyses, twenty-eight are ≥ 90% concordant and show a range of ages between ca. 1834 and 633 Ma (Th/U = 0.14–1.35). Of these twenty-eight analyses, six were selected for Lu–Hf isotope analysis. Most of the data have ^{206}Pb/^{238}U ages between 1016 and 931 Ma (Fig. 5b), with minor concentrations between ca. 895 and 746 and ca. 699 and 633 Ma. There are three Palaeoproterozoic (ca. 1834 Ma and 1741 Ma) and early Mesoproterozoic (ca. 1388 Ma) grains. The youngest grain has a ^{206}Pb/^{238}U age of 633 ± 20 Ma. The Th/U ratios do not correlate with age, nor is there any notable difference between CL-defined cores and rims (Fig. 3; Supplementary Table 1), making it unlikely that there was a distinct period of in-situ zircon growth. There is one very low Th/U ratio (0.01; analysis BU4_38), with a ^{206}Pb/^{238}U age of ca. 746 Ma. Overall, we suggest that the protolith of this sample is most likely to be a feldspathic sandstone, deposited after ca. 633 Ma.

Hafnium isotope analyses on the gneiss (six grains) gave ε_{Hf}(t) values ranging between +7.04 and +10.46, suggesting juvenile sources, with minimal continental crust involvement (Fig. 7a).

BU2 + BU6 Syenogranite (14°5'N 35°01'E and 14°37'N 35°01'E)

Thirty-nine analyses were conducted that included two core-rim pairs, though there was no discernible age difference between the cores and rims. Of these, eight grains were targeted for Lu–Hf isotope analyses. The ^{206}Pb/^{238}U weighted average plot shows a spread in ages from 841–712 Ma (n=15), with

four distinctly older analyses that are interpreted to represent inherited zircons. Seven zircon analyses are used to define an age plateau with coeval $^{206}Pb/^{238}U$ and $^{207}Pb/^{206}Pb$ ages with a weighted mean $^{206}Pb/^{238}U$ age of 756 ± 10 Ma (MSWD = 1.6). The $^{206}Pb/^{238}U$ and $^{207}Pb/^{206}Pb$ ages for the remaining four younger analyses diverge suggesting that these have been affected by lead loss (Fig. 5c). The $^{207}Pb/^{206}Pb$ ages of the youngest 11 analyses also yield an age of 775 ± 17 Ma, MSWD = 0.41, within error of the $^{206}Pb/^{238}U$ age. Although more precise, the progressive decrease in $^{206}Pb/^{238}U$ ages suggests that the more consistent $^{207}Pb/^{206}Pb$ age is the best estimate of crystallisation of the granite.

The $\varepsilon_{Hf}(t)$ values can be divided into two groups ($Hf_{(i)}$ = 0.28140–0.28251). One with predominately juvenile values ranging from +4.89 to +7.95, suggesting minor crustal involvement. The second group is defined by $\varepsilon_{Hf}(t)$ values between -31.12 and -17.30. These suggest that the parent magma was heterogeneous and involved some remelting of pre–existing continental crust (Fig. 7a).

Ouaddaï Region
OU1 Coarse – grained syenogranite (12°25'N 21°26'E)

Of the thirty-four analyses, only nine are ≤ 10 % discordant (targeting both rims and cores). For Lu–Hf isotope analysis four of these grains were analysed ($Hf_{(i)}$ 0.28226–0.28241). The $^{206}Pb/^{238}U$ weighted average plot (analyses ranging between 941–576 Ma; Th/U = 1.0–0.2) (Fig. 5d). The older analyses (942 ± 24 Ma, 866 ± 22 Ma and 816 ± 21 Ma) are defined by cores in CL and are interpreted to be inherited grains. The remaining analyses do not form a $^{206}Pb/^{238}U$ age plateau, suggesting that they experienced post-crystallisation lead loss and give a large MSWD of 19 from the calculated $^{206}Pb/^{238}U$ age of 618 ± 33 Ma. The $^{206}Pb/^{207}Pb$ age, however, yielded an age of 661 ± 27 Ma with a MSWD of 0.79 (n=6), which is interpreted as the best estimate of the crystallisation age of this pluton.

The $\varepsilon_{Hf}(t)$ values range between -0.58 and -4.96, suggesting these zircons are from a more evolved source (Fig. 7a).

OU2 Coarse – grained syenogranite (13°46'N 20°50'E)

Thirty-one zircons were analysed, with one core-rim pair (showing no age difference). Twelve of these analyses were ≤ 10% discordant and show a range of $^{206}Pb/^{238}U$ ages between 964–590 Ma (Th/U=0.07–1.36). Of these seven grains, nine were selected for Lu–Hf isotope analysis ($Hf_{(i)}$=0.28218–0.28244). The $^{206}Pb/^{238}U$ weighted average plot of analyses highlights one old grain (ca. 964 Ma) that is interpreted as an inherited zircon (Fig. 5e). The remainder range between 662 Ma and 590 Ma (Fig. 5e). No age difference was seen in the core-rim pair analysed (analyses 28 and 29) and with the exception of one analysis with very a low Th/U ratio, there is no evidence to suggest multiple generations of zircon. A weighted mean $^{206}Pb/^{238}U$ age of all the <700 Ma near concordant (≥ 90%) data gives an age of 618 ± 15 Ma with a large MSWD of 6 (n=11). It is suspected that this large MSWD is due to limited post-crystallisation Pb loss. Excluding one outlier at ca. 650 Ma, the $Hf_{(i)}$ values range between 0.28228–28231 and support the interpretation that these zircons have lost some Pb, decreasing in age but retaining the same $^{177}Hf/^{176}Hf$ composition (Supplementary Table 2; Supplementary Fig. 1). Therefore, a $^{207}Pb/^{206}Pb$ weighted mean of the same analyses was calculated, yielding an age of 653 ± 20 Ma (MSWD = 0.64). Just using the oldest three analyses (661–641 Ma) a similar $^{206}Pb/^{238}U$ age of 651 ± 11 (MSWD =1.07, n=3) is achieved. We suggest that the $^{207}Pb/^{206}Pb$ age is more representative of the data and the best estimate for the crystallisation age of this granitoid.

The $\varepsilon_{Hf}(t)$ values on five zircon grains (ca. 662–598 Ma), range between -2.65 and -4.47. One zircon at ca. 650 Ma has a positive $\varepsilon_{Hf}(t)$ value of +2.04. The interpreted inherited grain at ca. 964 Ma has a $\varepsilon_{Hf}(t)$ value of +0.17 (Fig. 7a).

OU3 Orthogneiss (12°38'N 21°20'E)

Of the thirty-two analyses, fourteen are ≥ 90% concordant and of these fourteen, eleven were selected for Lu–Hf isotope analysis. U–Pb analyses show a range of ages from 2753–978 Ma. The $^{206}Pb/^{238}U$ weighted average plot shows one distinct population that forms a plateau between 1031–978 Ma (Fig. 5f). The two distinctly older analyses ($^{207}Pb/^{206}Pb$ ages of 2753 ± 44 Ma and 1967 ± 53 Ma) are defined by distinct CL cores and are interpreted as inherited grains. The main population (defined by prismatic, oscillatory-zoned zircons), is made up of twelve zircons and yields a $^{206}Pb/^{238}U$ weighted mean age of

996 ± 12 Ma with an MSWD of 1.7. The ^{207}Pb/^{206}Pb weighted average of the same analyses gave an age of 1030 ± 18 Ma (MSWD=0.78, n=12). The ca. 1000–900 Ma grains have a Hf$_{(i)}$ ratio between 0.28233 and 0.28240 (Supplementary Fig. 1), showing little variability with decreasing age. Therefore, this likely suggests that the ^{206}Pb/^{238}U age represents a younger constraint and therefore the ^{207}Pb/^{206}Pb age is interpreted to be the best representation for the crystallisation age, with inheritance of grains at ca. 2753 and 1967 Ma.

The ε_{Hf}(t) values range between +8.74 and +6.01 (n=11) suggesting that these zircons were from a juvenile source, with little continental crust involvement. The two inherited grains at ca. 2753 and 1967 Ma have ε_{Hf}(t) values of -9.69 and -3.81 respectively, suggesting an evolved origin (Fig. 7a).

Central and Mayo Kebbi Region
CM1 Monzogranite (12°24'N 17°20'E) – Central Region

Forty-three analyses were conducted targeting cores and rims, of these eleven are ≤ 10% discordant. The analyses show a range of ^{206}Pb/^{238}U ages from 1011–535 Ma (Th/U = 0.66–1.13). Six (of eleven) were targeted for Lu–Hf isotope analysis. The U–Pb data (Supplementary Table 1) form a spread along the concordia (Fig. 5g), forming a cluster of ages between 600–550 Ma. The oldest analysis at ca. 1011 Ma is interpreted as an inherited grain (Fig. 3), the grain has rounded edges with faint oscillatory zonation. The next oldest analyses ca. 676 Ma is a core-rim pair and the corresponding rim (analysis 58), though slightly more than 10% discordant (11%), gives a younger age of ca. 574 Ma. Therefore, the ca. 676 Ma age is also excluded from the main calculation. The remaining analyses yield a ^{206}Pb/^{238}U weighted average age of 561 ± 14 Ma with a large MSWD of 7.9. The progressive reduction in ^{206}Pb/^{238}U age suggest that these zircons likely experienced Pb-loss. In this case, the oldest analyses likely reflect an age closer to crystallisation, giving a ^{206}Pb/^{238}U weighted average of 579 ± 15 Ma (MSWD=1.9; n=4). Similarly, a weighted average using the ^{207}Pb/^{206}Pb system of the youngest nine analyses, provides an older estimate of 594 ± 22 Ma (MSWD = 0.53, n=9). These are within uncertainty of each other and with relatively scattered data, are interpreted to provide the best estimate for the age of crystallisation of this monzogranite.

The $\varepsilon_{Hf}(t)$ values range between -4.69 and -20.22 (n=5). These negative values imply formation from the reworking of continental crust. The inherited grain at ca. 1011 Ma yields an $\varepsilon_{Hf}(t)$ of -14.20, similar to the values from the ca. 550 Ma grains (Fig. 7a).

CM2 Syenogranite (12°10'N 18°40'E) – Central Region

Of the thirty-three analyses, fifteen are ≤ 10% discordant and show a range of $^{206}Pb/^{238}U$ ages between 594–538 Ma (Th/U = 0.38–1.27). These analyses (Supplementary Table 1), though they show variations in age, sit within uncertainty of each other. Unfortunately, no Lu–Hf isotopes were collected for this sample. The youngest four analyses are located close to large cracks or represent a mixed age due to poor spot placement and have therefore been excluded from the age calculation (Fig. 5h). The main population of zircons is defined by eleven zircons made up of differing morphologies (Fig. 3). A weighted average of all these zircons yields a $^{206}Pb/^{238}U$ age of 580 ± 6 Ma with a MSWD of 2. The $^{207}Pb/^{206}Pb$ age gives a weighted average of 597 ± 23 Ma (MSWD=0.79, n=11). It is suspected that these likely have not remained in a completely closed system, with the oldest $^{206}Pb/^{238}U$ age (594 ± 14 Ma) within error of the calculated $^{207}Pb/^{206}Pb$ weighted average, and therefore the less precise older $^{207}Pb/^{206}Pb$ age is considered a more accurate estimate of the age of crystallisation.

MK1 Mylonitised granite (07°38'N 15°51'E) – Mayo Kebbi region

Of the ninety-three analyses, thirty-nine of these analyses are ≤ 10% discordant and show a range of $^{206}Pb/^{238}U$ ages from 649–550 Ma ((Supplementary Table 1; Th/U=0.41–1.15). Of these zircons, six were analysed for Lu–Hf isotopes. The $^{206}Pb/^{238}U$ weighted average plot shows a distinct trend decreasing from ca. 649 Ma, with the majority of the analyses at ca. 575 Ma (Fig. 5i). The older analyses are not defined by cores or differing morphologies and a weighted average of all analyses gives a $^{206}Pb/^{238}U$ age of 622 ± 16 Ma (n = 5; MSWD of 2.2). A younger population, excluding the oldest five analyses, yielding an age of 571 ± 4 Ma (MSWD of 1.7, n = 34). The older analyses have slightly different $Hf_{(i)}$ values (0.28174 and 0.28182) when comparted to the main population (0.28182–0.28186; Supplementary Table 2; Supplementary Fig. 1). This potentially suggests that these are inherited rather than Pb-loss (as

seen in other samples) and the crystallisation age for the granite is represented by the younger population at 571 ± 4 Ma.

The $\varepsilon_{Hf}(t)$ values range between -22.94 and -20.11 (n=6) suggesting these zircons were formed from the reworking of continental crust (Fig. 7a).

MK2 + MK3 Monzogranite (07°42'N 15°59'E and 07°38'N 15°53'E) – Mayo Kebbi region

Fifty-six analyses were conducted targeting both rims and cores (with no discernible age difference). Of these, twenty-one sit ≤10% from concordance and have a range of $^{206}Pb/^{238}U$ ages between 570–554 Ma (Th/U= 0.48–1.34). Ten grains were targeted for Lu–Hf isotope analysis. On the $^{206}Pb/^{238}U$ weighted average plot a distinct age plateau is seen (Fig. 5j) with similar $Hf_{(i)}$ ratios (0.28182–0.28190) (Supplementary Table 2; Supplementary Fig. 1). Twenty one analyses give a $^{206}Pb/^{238}U$ age of 556 ± 5 Ma with an MSWD of 1.6. This age is interpreted to represent the best estimate of the age of crystallisation.

The $\varepsilon_{Hf}(t)$ values for this sample give data between -19.42 and -22.02, suggesting these zircons were sourced from the remelting of continental crust (Fig. 5).

Zircon U–Pb geochronology—Metasedimentary Rocks
Butana:
BU3 Meta porphyritic andesite (15° 23' N 34° 41' E)

Twelve zircons were analysed and of these seven were ≤10% discordant, with a $^{206}Pb/^{238}U$ and $^{207}Pb/^{206}Pb$ age range between ca. 1839 Ma and 679 Ma (Fig. 6a). There are two main populations (n>3) of zircon within this sample: ca. 1837 Ma and ca 973 Ma, with the youngest grain yielding a $^{206}Pb/^{238}U$ age of 679 ± 16 Ma. The youngest population of zircons gives a $^{206}Pb/^{238}U$ weighed average of 973 ± 14 Ma (MSWD =0.34). It is interpreted that the youngest grain represents a maximum depositional age constraint at ca. 679 Ma, which may reflect the age of the volcanic source to this metamorphosed lithic arenite.

Seven Lu–Hf analyses were conducted on the main age populations identified in the U–Pb data (Fig. 7b). Grains with $^{207}Pb/^{206}Pb$ age ages between ca. 1853 to 1820 Ma have $\varepsilon_{Hf}(t)$ values that range from

-8.21 to-6.61 (n=3). Analyses that yield ^{206}Pb/^{238}U ages between ca. 981 and 968 Ma have values between +8.68 and +6.45. One grain at 679 Ma give an ε_{Hf}(t) value of +4.42

Ouaddaï Region
OU4 chloritized mica phyllite schist (12° 13'N 21° 22'E)

Thirty-seven zircon grains were analysed and of these fourteen are ≥90% concordant. These give a ^{206}Pb/^{238}U age range between ca. 1052–602 Ma, with the main data peaks at ca. 1010 Ma, ca. 690 Ma and 604 Ma (Fig. 6b). The youngest population yields a ^{206}Pb/^{238}U weighted average age of 609 ± 24 Ma (MSWD=1.8, n=3). The youngest grain returned a ^{206}Pb/^{238}U age of 602 ± 14 Ma and is interpreted to represent the maximum depositional age for this dataset.

Fifteen zircons were analysed for Lu–Hf isotopes and these give a ε_{Hf}(t) range between -14.45 and 10.95 (Fig. 7b). Zircons with ^{206}Pb/^{238}U ages between 1052–969 Ma have ε_{Hf}(t) values between -14.45 and -11.10 (n=8). Zircons with an age range between ca. 721 and 687 Ma have ε_{Hf}(t) values between +10.95 and +9.05 (n=4). Lastly, zircons with ages between ca. 621 and 601 Ma have a ε_{Hf}(t) range of -4.49 and -3.62 (n=3).

OU5 Muscovite schist 12° 10' N 21° 13' E)

Of thirty-four analyses, twenty-nine were ≤10% discordant and have a ^{206}Pb/^{238}U and ^{207}Pb/^{206}Pb age range between ca. 2648 and ca. 976 Ma (Fig. 6c). There are three age peaks, in the kernel density estimate plots, at ca. 2648 Ma, ca. 1970 Ma and ca. 1082 Ma. The youngest population gives a weighted average ^{206}Pb/^{238}U age of 987 ± 10 Ma (n=6; MSWD=0.69) and the youngest grain yields a ^{206}Pb/^{238}U age of 967 ± 27 Ma. The youngest grain is used to interpret the best estimate from this data of the maximum depositional age.

Ten grains were analysed for Lu–Hf isotopes (Fig. 7b) from each of the main peaks defined by the kernel density estimate plots (Fig 7b). The zircons with ^{206}Pb/^{238}U ages between 1088–976 Ma have ε_{Hf}(t) values between -14.17 to -1.11 (n=7). Two grains at ca. 1992 Ma and 1937 Ma have ε_{Hf}(t) values of −3.25 and -4.72, respectively. One grain at ca. 2648 Ma has an ε_{Hf}(t) value of 1.65.

Central and Mayo Kebbi Region
CM3 Garnet-bearing psammitic gneiss (12° 24' N 17° 43'E)

Forty zircon grains were analysed and seventeen are ≤90% concordant and have a ^{206}Pb/^{238}U age range between 964 Ma and 584 Ma. There is a scattering of data between 964–933 Ma, 855–712 Ma, and 696–584 Ma (Fig. 6d). The spread in data makes it difficult to calculate a population (n≥3), with the nearest population at 689 ± 27 Ma (n=3, MSWD=1.7). The single youngest near-concordant grain, with a ^{206}Pb/^{238}U age of 584 ± 15 Ma, is interpreted as the maximum depositional age.

The Lu–Hf isotopes (in zircon) were done on eight grains with a ε_{Hf}(t) spread from 10.64 to -4.36 (Fig. 7b). Zircons with ^{206}Pb/^{238}U ages between 964–933 Ma have ε_{Hf}(t) values of +6.4 (n=1), ca. 855–712 Ma have ε_{Hf}(t) values between +10.64 to -3.3 (n=4), and 696–584 Ma have ε_{Hf}(t) values between +9.71 to -4.36.

DISCUSSION
Timing and nature of magmatism and sedimentation in Butana
The timing and nature of magmatism in Butana is largely unknown, to date there has been little geological work done in this area. However, Butana holds an important position close to the transition between the enigmatic Saharan Metacraton and the accreted terranes of the Arabian Nubian Shield (Abdelsalam et al., 2002; Fritz et al., 2013; Johnson, 2014; Johnson et al., 2011). The terrane is composed of low-grade metavolcanic rocks, pre- and syn-tectonic granitic intrusions, serpentinites, ophiolitic metagabbro and high-grade metamorphic rocks. This paper highlights that the magmatism in the Butana occurs at ca. 839 Ma and 775 Ma (Table 2 and 3). The first pulse is defined by radiogenic melts, defined by ε_{Hf}(t) values (+6.59 to +11.25), suggesting that these zircons crystallised from a melt with minimal assimilation of older continental crust (Fig. 7a). Slightly west, a granite (BU2 + BU6) has a crystallisation age of 775 ± 17 Ma, with ε_{Hf}(t) values between +8 and -31, with similar aged zircons showing both evolved and juvenile signatures (Figs. 5 and 7a). A possible explanation for the bimodal ε_{Hf}(t) signature could be that the magma was heterogeneous and contained xenoliths of the older, evolved Saharan Metacraton (in a similar way to that described by Tang et al., 2014). These evolved ε_{Hf}(t) signatures overlap with known Saharan Metacraton samples analysed in this study (Fig. 7a, OU1, OU2, OU3, CM1, CM2, MK1 and MK2+MK3).

Juvenile magmatism occurred in Butana at ca. 839 Ma, synchronous with magmatism seen throughout the Arabian Nubian Shield, for example in Western Ethiopia (Blades et al., 2015) and Saudi Arabia (Robinson et al., 2014). The occurrence of both evolved and juvenile $\varepsilon_{Hf}(t)$ signatures at ca. 787 Ma, implying the incorporation of country rock, either suggests that a previously exotic Butana accreted onto the Saharan Metacraton before ca. 775 Ma, or that ca. 839 Ma magmatism simply did not record a continental signature.

Though statistically insignificant, the metasedimentary rocks preserve late Cryogenian or Ediacaran maximum depositional ages, providing some insight into the sedimentation in the region. Meta-volcaniclastic sample (BU3) preserves detrital zircons at ca. 1800 Ma and ca 970 Ma, giving an indication of which terranes formed the source for these sediments (Figs. 6a, 7b and 8a). The few grains at ca. 970 have juvenile hafnium isotope signatures (+8.68 and +6.45) and are similar to the main age group preserved in the paragneiss sample (BU4+BU5) that range in age between 1051–931 Ma (+6.9 to +11.25). Butana is located directly west of the largely juvenile Arabian Nubian Shield, so this region must be considered a possible source. However, most of the Arabian Nubian Shield formed after 970 Ma and little evidence of Palaeoproterozoic crust exists west of the Afif terrane of Saudi Arabia (Fig. 8a). Alternatively, these sediments may be sourced from juvenile igneous rocks from within the Saharan Metacraton. For example, sample OU3, in the Ouaddaï region, this granite has an age of ca. 1030 Ma (+8.72 to +6.0) and other Mesoproterozoic ages have been reported in these areas, though little work has been done on them (Penaye et al., 2006; Shellnutt et al., 2017; Shellnutt et al., 2018). Possible sources for the older ca. 1837–1834 Ma, ca. 1741 Ma and 1388 Ma grains, are likely found within the Saharan Metacraton (Fig. 8a and b). Terranes in the east of the Arabian Nubian Shield, such as the Khida terrane, the Yemini Abas and Al Mahfid terranes (Stoeser and Stacey, 1988; Stoeser et al., 2001; Whitehouse et al., 2001) have ages and hafnium isotopes that are similar to the Butana detritus. The maximum depositional ages of the Butana sedimentary protoliths (down to ca. 630 Ma) do not discount eastern sources, as the younger sutures within the Arabian Nubian Shield, such as the Keraf and Nabitah Sutures may have closed before deposition of these protoliths (Johnson et al., 2011; Küster et al., 2008;

Robinson et al., 2014). However, these eastern sources are a couple of thousand kilometres away and are much less likely than the adjacent Saharan Metacraton.

Timing and nature of magmatism and sedimentation in Chad

The Ouaddaï region lies in the east of Chad and has basement comprised of granitoids, migmatites and gneisses (Fig. 1a and b). The granitoids protolith of a gneiss sample (OU3) from the Ouaddaï region (Table 2) yields a crystallisation age of 1030 ± 18 Ma, with inheritance of grains at 2753 ± 22 Ma and 1967 ± 26 Ma. Despite the inherited grains, the $\varepsilon_{Hf}(t)$ for the ca. 1030 Ma population is juvenile (Fig. 7a; +8.72 to +6.55). The inherited grains show derivation from even older reworked continental crust ($\varepsilon_{Hf}(t)$ = -13.52 to -11.29). The samples collected from two coarse grained monzonites that intrude the older gneiss, show that magmatism occurring between ca. 670–630 Ma, with $\varepsilon_{Hf}(t)$ values, +2.04 and -4.07 suggesting interaction with older continental crust (Fig. 7a).

Monzogranitic magmatism in the Chadian Central Massif is dated here at ca. 600–590 Ma (sample CM2 and CM1). Hafnium isotopes preserve significant continental crustal influence ($\varepsilon_{Hf}(t)$ = -4.69 and -20.22), interpreted as representing melting of older Saharan Metacraton. Shellnutt et al. (2020) dated a series of ferroan and magnesian alkali to calc-alkali rocks between ca. 600–580 Ma from the Central Massif. These authors also demonstrated the evolved nature of the rocks and interpreted the granitoids to represent an Ediacaran continental arc.

The southernmost exposures of Precambrian rocks in Chad, consist of granitoids that have ages coeval with the Central Massif, though younger than those from the Ouaddaï region (Fig. 7a). Here, in Mayo Kebbi, the oldest ages (ca. 571 Ma) are from deformed granitoids that are within error of magmatism in the Central Massif. These are similar to previously dated samples of the Zabili pluton from the same region, where a crystallisation age of 567 ± 10 Ma (Isseini et al., 2012) was obtained. These rocks also record earlier Neoproterozoic inherited zircons similar to the samples dated here. Younger undeformed monzogranite magmatism crystallised at 556 ± 5 Ma. The $\varepsilon_{Hf}(t)$ values from these rocks are between -19.42 and -22.94, suggesting that these zircons were sourced from a magma that involved the remelting of the older Saharan Metacraton. These ages compare with an older study that used the $^{207}Pb/^{206}Pb$

zircon evaporation technique to date late-stage porphyritic granitoids in the region at 570 ± 1 Ma (Penaye et al., 2006), suggesting that deformation was broadly coeval with magmatism at ca. 571 Ma. The metasedimentary samples analysed here from Chad (Table 3), are poor in detrital zircon, making it difficult to place much emphasis on the data. Regardless, the age of zircons that are present are important in understanding tential sources for the protolith sediments. The samples from the Ouaddaï region (OU5 and OU4) have very different maximum depositional ages and may represent different original sedimentary packages. However, both contain zircon populations that range between 1088–976 Ma with unradiogenic Lu–Hf signatures (Fig. 7b; ε_{Hf}(t) -14.45 to -1.11). There is no known source for these zircons. Similar-aged granites analysed in this study from the Ouaddaï region have much more radiogenic Lu–Hf isotopic values (ε_{Hf}(t) =+8.72 to +6.01). The only known similar zircon from the central Saharan Metacraton is an interpreted inherited grain from a magmatic sample in the Central Massif (ca. 1011 Ma; sample CM1), which yielded a similar ε_{Hf}(t) value of -14.2 (Fig. 7a). This demonstrates that there is crust of this age and hafnium composition in the region, just that none has been analysed yet. Interestingly, the younger of the two metasedimentary samples (OU4) contains a population of zircons between ca. 721 and 687 Ma with positive ε_{Hf}(t) values (+9.04 to +10.95), suggesting that the source of these zircons had very little crustal input (i.e. mantle derived). Similar-aged igneous rocks, with similar radiogenic Lu–Hf isotopic values occur in the Arabian Nubian Shield (Fig. 8) to the east (Ali et al., 2015; Ali et al., 2013; Ali et al., 2016; Robinson et al., 2017; Robinson et al., 2015a, b; Robinson et al., 2014). The Arabian Nubian Shield is a considerable distance from these rocks (Fig. 1). Alternatively, the Mayo Kebi region to the south (Fig. 1) contains deformed diorites that are broadly the same age as these detrital zircons, with juvenile whole-rock Nd isotope values (Penaye et al., 2006).

The younger, Ediacaran detrital zircons (ca. 621–601 Ma) have a Lu–Hf signature (ε_{Hf}(t) = -4.49 to +3.62) that likely reflects local derivation, from the Saharan Metacraton, shown by the samples analysed in this study.

In the Central and Mayo Kebbi regions the only analysed early Neoproterozoic grain (ca. 963 Ma) has a juvenile ε_{Hf}(t) value, similar to the granitoid (OU3) sampled from the Ouaddaï region. The analyses with ages between ca. 855 Ma and ca. 758 Ma have radiogenic Lu–Hf and could reflect far-travelled sources

from the Arabian Nubian Shield, or the Oubanguides (Fig. 8a and 8b). Alternatively, the may be locally sourced. Penaye et al. (2006) reported U–Pb zircon ages of ca. 740 Ma with Sm–Nd values for gabbroic to dioritic rocks— analyses presented here are older, but the zircon Pb-evaporation technique used by Penaye et al. (2006) only can yield minimum ages for the analysed zircons. One grain at ca. 712 Ma yields a negative ε_{Hf}(t) value (-3.33), negative values of this age are seen in sample BU2+BU6, though these analyses are much more evolved (-13.93 to -31.1). No other possible sources are known. However, the paucity of data from the Saharan Metacraton make it quite possible that sources exist in the region.

Implications for the tectonic geography for the Saharan Metacraton

Throughout the literature there have a number of interpretations for the formation of the basement beneath the Sahara, these are summarised in Abdelsalam et al. (2002). The main hypotheses are: 1) That a craton existed prior to the Neoproterozoic. The lithospheric root later delaminated, and the region became 'decratonised'. 2) There was coherent continental crust prior to the Neoproterozoic, which rifted in the Neoproterozoic to form oceanic basins that later closed and led to continent collisions in the region. 3) Lastly, this tract is made up of a collage of exotic terranes that were assembled during the Neoproterozoic (this last model reinvigorated by Şengör et al., 2020).

The eastern margin of the Saharan Metacraton is typically defined by the Keraf Suture, which has juxtaposed the younger, juvenile arc terranes of the Arabian Nubian Shield against Mesoproterozoic rocks of the eastern Saharan Metacraton (Abdelsalam et al., 2002; Küster et al., 2008) . The variation in age data throughout northern Africa, shown in Fig. 8a, highlight the remobilisation of the Saharan MetacratonSaharan Metacraton during the Neoproterozoic, as well as a definable change from juvenile younger rocks to predominantly older crust (Fig. 8b). Little U–Pb data exist within the Saharan MetacratonSaharan Metacraton, the majority of data being older whole rock Rb–Sr results. However, a more recent compilation (de Wit and Linol, 2015) suggests that the southern parts of the region may be composed of late Mesoproterozoic crust (Fig. 8). However, these ages remain untested due to the isotopic data remaining unpublished. In the west, Archaean to Palaeoproterozoic crust dated to

between 2629–1922 Ma (Liégeois et al., 1994; Stern, 1994; Sultan et al., 1994) dominates. These rocks are intruded by late Mesoproterozoic granites (ca. 1100–1000 Ma), which were deformed during the Neoproterozoic.

Data presented here from granitoids from the Ouaddaï region demonstrate the presence of ca. 1000 Ma juvenile magmatism in this part of the core of the Saharan Metacraton. Inherited zircons in the southern Mayo Kebbi region published here and from the Guéra Massif by Shellnutt et al. (2017) demonstrate that this much of the southern Saharan Metacraton may be underlain by juvenile Stenian crust. Evidence for juvenile magmatism of this age is not known from northern Cameroon, although detrital zircons in the Neoproterozoic Poli and Lom basins suggest that it exists within the region (Toteu et al., 2006). Stenian crust may be limited to Chad and the Sudan. The occurrence of possible Mesoproterozoic rocks, outside the Kibaran belt, are very limited in western Central Africa, the most significant that have been reported are granites in the south-western part of Central African Republic (Censier 1991) interpreted to reflect a post-Kibaran and pre-Gondwana forming extensional event (Vicat et al., 2001). Unfortunately, these have only been dated by the whole-rock Rb–Sr technique. Similar-aged granites, dated around 1000 Ma, are also known in the West-Congolian area along a fault bordering the Mayombe rift (Vicat et al., 2001). We suggest that the Stenian juvenile magmatism that we record supports the conclusion of de Wit and Linol (2015) that a significant area of the southwest Saharan Metacraton is made up of late Mesoproterozoic volcanic arc crust.

The next known phase of magmatism is present in the Mayo Kebbi area at ca. 737–723 Ma. This magmatism has been interpreted as part of a juvenile arc, due to their calc-alkaline chemistry and juvenile nature (Penaye et al. 2006). Penaye et al. (2006) also suggested that this Mayo Kebbi region formed a separate late Tonian volcanic arc terrane that collided and amalgamated with the southern Adamawa-Yadé Terrane. These authors also suggested that the boundary between the Adamawa-Yadé and Mayo Kebbi Terranes could be traces northwards into Chad as a prominent gravity anomaly, known as the Chad Lineament (Liégeois et al., 2013). This boundary was inferred to separate the Mayo Kebbi region from the Central and Ouaddaï outcrop regions with a suggestion that these Chadian regions may correlate with the Cameroonian Adamawa-Yadé Terrane (Penaye et al., 2006).

The Ouaddaï Region preserves evidence of magmatism between 654–610 Ma, with inheritance and Lu–Hf isotope values showing the incorporation and existence of older crust that is consistent with the Stenian rocks dated from the region. Ediacaran magmatism (ca. 600–580 Ma) in the Central Massif contains inherited Stenian-aged zircons (this study, Shellnutt et al., 2020). The $\varepsilon_{Hf}(t)$ values from this region stretch to much more negative values than those from the Ouaddaï region, suggesting the presence of Archaean/Palaeoproterozoic crust here. Crust of this age has been reported from the Adamawa-Yadé Terrane (Tchakounté et al., 2017). Cryogenian magmatism has also been reported from the Mayo Kebbi Region (ca. 665–640 Ma), which has been interpreted to be coeval with amalgamation of the Mayo Kebbi Terrane and the Adamawa-Yadé Terrane (Penaye et al., 2006).

Later magmatism in Mayo Kebbi (ca. 575–550 Ma, this study; Shellnutt et al., 2018)(Fig. 8) preserves $\varepsilon_{Hf}(t)$ values that also show significant incorporation of older crust in the parent magmas ($\varepsilon_{Hf}(t)$= -14 to -22) and model ages, similar to those from the Central region, but much older than those of the Ouaddaï region (ca. 3–2 Ga). We suggest that the coupled U–Pb and hafnium isotope data suggest that both Mayo Kebbi and the Central Massif lay on similar crust by the Ediacaran, with evidence of older crust extending back to at least the Palaeoproterozoic. In contrast, the Ouaddaï region preserves much less evidence of crustal inheritance prior to the late Mesoproterozoic. The similarities between the Central Massif and the Mayo Kebbi region indicate that if the Chad Lineament was a major terrane boundary, it had sutured before the Ediacaran magmatism reported here. We suggest that it is likely that by ca. 575 Ma, these regions were juxtaposed, and both overlay crust with evolved isotopic signatures. The isotopic distinction between the Central Massif and the Ouaddaï Massif is much more distinct, with hafnium isotopes demonstrating the much more juvenile, late Mesoproterozoic, nature of the Ouaddaï region. Limited older Proterozoic inherited zircon does occur in the Ouaddaï, though, and the characteristic Stenian magmatism of the Ouaddaï is also indicated to occur in the Central Massif by the presence of inherited zircon in this region. The lack of exposure throughout the area and limited research still leaves open the possibility that these regions all lay on the same terrane. In this model, an Archaean/Palaeoproterozoic core in the west (that may be the Adamawa-Yadé Terrane) was intruded by voluminous Stenian magmatism, possibly during extension in a supra-subduction setting in

the east. Alternatively, the three regions may represent three different terranes that did not amalgamate until the later Neoproterozoic—evidence of this amalgamation being buried below the intervening basins.

Seismic tomography presented in Abdelsalam et al. (2011), shows the Saharan Metacraton to have an upper mantle structure that can be explained by partial removal of its cratonic root, and a sub continental lithospheric mantle typical of other cratons persisting to depths of 100 km. Ediacaran magmatism between 600–560 Ma, seen in this study is abundant throughout the entire north-eastern Saharan metacraton, with exception of the Uweynat massif (Abdelsalam et al., 2002; Küster and Harms, 1998; Stern, 1994), as well as on the western border of the Saharan Metacraton, in association with the Raghane shear zone (Abdallah et al., 2007; Henry et al., 2009; Liégeois et al., 1994). To the south, in central and southern Cameroon, there are also late Neoproterozoic to early Cambrian rocks, which pervasively intrude domains (Bessoles, 1980; Ganwa et al., 2018; Ganwa et al., 2016) and these are usually associated with regional shear zones. We speculate that this vast region of Ediacaran to Cambrian post-tectonic magmatism may reflect the loss of the cratonic root throughout this region.

The terranes in Butana have been interpreted to form as an accreted arc terrane to the east of a continental mass (i.e. Saharan Metacraton), with the oldest juvenile magmatism at ca. 840 Ma and subsequent magmatism at ca. 787 Ma. Magmatism and metamorphism at ca. 790–780 Ma are also seen in western Ethiopia, in the Dire Dawa Basement in eastern Ethiopia as well as in the Tokar/Barka Terrane (Andersson et al., 2006; Blades et al., 2015; Teklay et al., 2003; Yeshanew et al., 2017). The bimodal $\varepsilon_{Hf}(t)$ signature and model ages, in the western most sample (BU2 + BU6) in Butana (Fig. 7a) suggest that when this granite crystallised, the magma assimilated older continental crust. This suggests that the terrane had accreted onto the Saharan Metacraton at this time and the presence of Palaeoproterozoic and Mesoproterozoic grains in the metasediments means that it was at least depositionally connected by the late Neoproterozoic (ca. 630 Ma). The juvenile rocks in the Bayuda Desert reported by Küster and Liégeois (2001) have also been interpreted to represent the eastern margin of the Saharan Metacraton. It is interpreted that the Keraf suture was a result of a sinistral transgressive tectonic regime that was a result of the closing of the Mozambique Ocean (Fig. 8), with

deformation along the shear zone ending at ca. 580 Ma and the terranes of the Arabian Nubian Shield amalgamated on the eastern margin of the Saharan Metacraton (Abdelsalam et al., 1998; Merdith et al., 2017; Merdith et al., 2020).

CONCLUSIONS

The relative timing and duration of Neoproterozoic magmatism within northern Africa is slowly being unravelled as geochronological and geochemical studies occur. We present new U–Pb, Hf isotopic data from zircons from the Butana region of the Sudan and from the Mayo Kebbi, Central Massif and Ouaddaï regions of Chad. This contribution highlights that magmatism in the Butana is defined by two main pulses; ca. 839 Ma and 775 Ma. Data suggest that formation of the Butana terrane began at ca. 839 Ma, from a mantle derived source. The younger pulse of magmatism shows evidence for the interaction between the juvenile terrane and older reworked continental crust. This is interpreted to reflect the accretion of Butana onto the Saharan Metacraton at this time (i.e. ca. 775 Ma).

The Ouaddaï region preserves juvenile Stenian magmatism, demonstrating the importance of volcanic-arc development in this area at the end of the Mesoproterozoic. Older crust does occur here and is seen by the presence of inherited zircon with the granitoids. It is possible that these zircons were detrital zircon in the country rock as no direct evidence for pre Stenian igneous rocks are preserved here. Cryogenian magmatism is also reported from the Ouaddaï region and dated between 654–610 Ma.

The Central Massif preserves Ediacaran magmatism that contain inherited Stenian-aged zircons that may indicate a link with Ouaddaï. However, unlike Ouaddaï, hafnium isotopes demonstrate the presence old Archaean/Palaeoproterozoic crust in this region that is also seen in the isotopic data from Ediacaran plutons in Mayo Kebbi in the far south of Chad. We suggest that the data are consistent with the Mayo Kebbi Terrane being thrust south over a continental fragment that dated back to the Archaean/Palaeoproterozoic (the Central Massif—the Adamawa-Yadé Terrane?) along the Chad Lineament after Tonian formation of the terrane and before Ediacaran magmatism in Mayo Kebbi. The evolved nature of Ediacaran magmatism in Mayo Kebbi is explained by partial assimilation of this ancient underthrust terrane.

REFERENCES

Abdallah, N., Liégeois, J.-P., De Waele, B., Fezaa, N., and Ouabadi, A., 2007, The Temaguessine Fe-cordierite orbicular granite (Central Hoggar, Algeria): U–Pb SHRIMP age, petrology, origin and geodynamical consequences for the late Pan-African magmatism of the Tuareg shield: Journal of African Earth Sciences, v. 49, no. 4-5, p. 153-178.

Abdelsalam, M. G., Abdel-Rahman, E., -S.M., El-Faki, E.-F. M., Al-Hur, B., El-Bashier, F.-R. M., Stern, R. J., and Thurmond, A. K., 2003, Neoproterozoic deformation in the northeastern part of the Saharan Metacraton, northern Sudan: Precambrian Research, v. 123, p. 203-221.

Abdelsalam, M. G., Gao, S. S., and Liégeois, J.-P., 2011, Upper mantle structure of the Saharan Metacraton: Journal of African Earth Sciences, v. 60, no. 5, p. 328-336.

Abdelsalam, M. G., Liegeois, J. P., and Stern, R. J., 2002, The Saharan Metacraton: Journal of African Earth Sciences, v. 34, no. 3-4, p. 119-136.

Abdelsalam, M. G., and Stern, R. J., 1996, Sutures and shear zones in the Arabian-Nubian Shield: Journal Of African Earth Sciences, v. 23, no. 3, p. 289-310.

Abdelsalam, M. G., Stern, R. J., Copeland, P., El-Faki, E.-F. M., Al-Hur, B., and Ibrahim, F. M., 1998, The Neoproterozoic Keraf Suture in NE Sudan: sinistral transpression along the eastern margin of West Gondwana: Journal of Geology, v. 106, p. 133-147.

Abu-Alam, T., Hassan, M., Stüwe, K., Meyer, S., and Passchier, C., 2014, Multistage tectonism and metamorphism during Gondwana collision: Baladiyah complex, Saudi Arabia: Journal of Petrology, v. 55, no. 10, p. 1941-1964.

Abu-Alam, T. S., and Hamdy, M. M., 2014, Thermodynamic modelling of Sol Hamed serpentinite, South Eastern Desert of Egypt: implication for fluid interaction in the Arabian–Nubian Shield ophiolites: Journal of African Earth Sciences, v. 99, p. 7-23.

Acef, K., Liégeois, J. P., Ouabadi, A., and Latouche, L., 2003, The Anfeg post-collisional Pan-African high-K calc-alkaline batholith (Central Hoggar, Algeria), result of the LATEA microcontinent metacratonization: Journal of African Earth Sciences, v. 37, no. 3-4, p. 295-311.

Ali, K. A., Kröner, A., Hegner, E., Wong, J., Li, S.-Q., Gahlan, H. A., and El Ela, F. F. A., 2015, U–Pb zircon geochronology and Hf–Nd isotopic systematics of Wadi Beitan granitoid gneisses, South Eastern Desert, Egypt: Gondwana Research, v. 27, no. 2, p. 811-824.

Ali, K. A., Wilde, S. A., Stern, R. J., Moghazi, A.-K. M., and Ameen, S. M., 2013, Hf isotopic composition of single zircons from Neoproterozoic arc volcanics and post-collision granites, Eastern Desert of Egypt: Implications for crustal growth and recycling in the Arabian-Nubian Shield: Precambrian Research, v. 239, p. 42-55.

Ali, K. A., Zoheir, B. A., Stern, R. J., Andresen, A., Whitehouse, M. J., and Bishara, W. W., 2016, Lu–Hf and O isotopic compositions on single zircons from the North Eastern Desert of Egypt, Arabian–Nubian Shield: Implications for crustal evolution: Gondwana Research, v. 32, p. 181-192.

Andersson, U. B., Hogdahl, K., Sjostrom, H., and Bergman, S., 2006, Multistage growth and reworking of the Palaeoproterozoic crust in the Bergslagen area, southern Sweden: evidence from U-Pb geochronology: Geological Magazine, v. 143, no. 5, p. 679-697.

Andresen, A., Augland, L., Boghdady, G., Lundmark, A., Elnady, O., Hassan, M., and El-Rus, M. A., 2010, Structural constraints on the evolution of the Meatiq gneiss dome (Egypt), east-African orogen: Journal of African Earth Sciences, v. 57, no. 5, p. 413-422.

Augland, L. E., Andresen, A., and Boghdady, G. Y., 2012, U–Pb ID-TIMS dating of igneous and metaigneous rocks from the El-Sibai area: time constraints on the tectonic evolution of the Central Eastern Desert, Egypt: International Journal of Earth Sciences, v. 101, no. 1, p. 25-37.

Avigad, D., Stern, R., Beyth, M., Miller, N., and McWilliams, M., 2007, Detrital zircon U–Pb geochronology of Cryogenian diamictites and Lower Paleozoic sandstone in Ethiopia (Tigrai): age constraints on Neoproterozoic glaciation and crustal evolution of the southern Arabian–Nubian Shield: Precambrian Research, v. 154, no. 1-2, p. 88-106.

Azzouni-Sekkal, A., Liegeois, J. P., Bechiri-Benmerzoug, F., Belaidi-Zinet, S., and Bonin, B., 2003, The "Taourirt" magmatic province, a marker of the closing stage of the Pan-African orogeny in the Tuareg Shield: review of available data and Sr-Nd isotope evidence: Journal of African Earth Sciences, v. 37, no. 3-4, p. 331-350.

Be'eri-Shlevin, Y., Eyal, M., Eyal, Y., Whitehouse, M. J., and Litvinovsky, B., 2012, The Sa'al volcano-sedimentary complex (Sinai, Egypt): A latest Mesoproterozoic volcanic arc in the northern Arabian Nubian Shield: Geology, v. 40, no. 5, p. 403-406.

Bendaoud, A., Ouzegane, K., Godard, G., Liégeois, J.-P., Kienast, J.-R., Bruguier, O., and Drareni, A., 2008, Geochronology and metamorphic PTX evolution of the Eburnean granulite-facies metapelites of Tidjenouine (Central Hoggar, Algeria): witness of the LATEA metacratonic evolution: Geological Society, London, Special Publications, v. 297, no. 1, p. 111-146.

Bessoles, B., 1980, GEOLOGIE DE L'AFRIQUE, LA CHAINE PANAFRICAINE" ZONE MOBILE D'AFRIQUE CENTRALE (PARTIE SUD) ET ZONE MOBILE SOUDANAISE".

Black, R., Latouche, L., Liégeois, J. P., Caby, R., and Bertrand, J. M., 1994, Pan-African displaced terranes in the Tuareg shiled (central Sahara): Geology, v. 22, p. 641-644.

Black, R., and Liegeois, J. P., 1993, Cratons, Mobile Belts, Alkaline Rocks and Continental Lithospheric Mantle - the Pan-African Testimony: Journal Of the Geological Society, v. 150, no. Pt1, p. 89-98.

Blades, M. L., Alessio, B. L., Collins, A. S., Foden, J., Payne, J. L., Glorie, S., Holden, P., Thorpe, B., and Al-Khirbash, S., 2019, Unravelling the Neoproterozoic accretionary history of Oman, using an array of isotopic systems in zircon: Journal of the Geological Society, p. jgs2018-2125.

Blades, M. L., Collins, A. S., Foden, J., Payne, J. L., Xu, X. C., Alemu, T., Woldetinsae, G., Clark, C., and Taylor, R. J. M., 2015, Age and hafnium isotopic evolution of the Didesa and Kemashi Domains, western Ethiopia: Precambrian Research, v. 270, p. 267-284.

Caby, R., 1987, The Pan-African belt of West Africa from the Sahara desert to the Gulf of Benin: Anatomy of Mountain Ranges, v. 1, p. 129-170.

Collins, A., and Pisarevsky, S., 2005, Amalgamating eastern Gondwana: The evolution of the Circum-Indian Orogens: Earth-Science Reviews, v. 71, no. 3-4, p. 229-270.

Cox, G. M., Lewis, C. J., Collins, A. S., Halverson, G. P., Jourdan, F., Foden, J., Nettle, D., and Kattan, F., 2012, Ediacaran Terrane Accretion in the Arabian-Nubian Shield: Gondwana Research, v. 21, p. 341-352.

de Wit, M. J., and Linol, B., 2015, Precambrian Basement of the Congo Basin and Its Flanking Terrains, in de Wit, M. J., Guillocheau, F., and de Wit, M. C. J., eds., Geology and Resource Potential of the Congo Basin: Berlin, Heidelberg, Springer Berlin Heidelberg, p. 19-37.

El Makkrouf, A. A., 1988, Tectonic interpretation of Jabal Eghei area and its regional application to Tibesti orogenic belt, south central Libya (SPLAJ): Journal of African Earth Sciences (and the Middle East), v. 7, no. 7-8, p. 945-967.

Fezaa, N., Liégeois, J.-P., Abdallah, N., Cherfouh, E. H., De Waele, B., Bruguier, O., and Ouabadi, A., 2010, Late Ediacaran geological evolution (575–555 Ma) of the Djanet Terrane, Eastern Hoggar, Algeria, evidence for a Murzukian intracontinental episode: Precambrian Research, v. 180, no. 3-4, p. 299-327.

Fritz, H., Abdelsalam, M., Ali, K. A., Bingen, B., Collins, A. S., Fowler, A. R., Ghebreab, W., Hauzenberger, C. A., Johnson, P., Kusky, T., Macey, P., Muhongo, S., Stern, R. J., and Viola, G., 2013, Orogen

styles in the East Africa Orogens: A review of the Neoproterozoic to Cambrian Tectonic Evolution: Journal of African Earth Sciences, v. 86, p. 65-106.

Ganwa, A. A., Klötzli, U. S., Diguim Kepnamou, A., and Hauzenberger, C., 2018, Multiple Ediacaran tectono-metamorphic events in the Adamawa-Yadé Domain of the Central Africa Fold Belt: Insight from the zircon U–Pb LAM-ICP-MS geochronology of the metadiorite of Meiganga (Central Cameroon): Geological Journal, v. 53, no. 6, p. 2955-2968.

Ganwa, A. A., Klötzli, U. S., and Hauzenberger, C., 2016, Evidence for Archean inheritance in the pre-Panafrican crust of Central Cameroon: Insight from zircon internal structure and LA-MC-ICP-MS UPb ages: Journal of African Earth Sciences, v. 120, p. 12-22.

Ghuma, M. A., and Rogers, J. J., 1978, Geology, geochemistry, and tectonic setting of the Ben Ghnema batholith, Tibesti massif, southern Libya: Geological Society of America Bulletin, v. 89, no. 9, p. 1351-1358.

Griffin, W., Pearson, N., Belousova, E., and Saeed, A., 2006, Comment: Hf-isotope heterogeneity in zircon 91500: Chemical Geology, v. 233, no. 3-4, p. 358-363.

Griffin, W. L., Wang, X., Jackson, S. E., Pearson, N. J., O'Reilly, S. Y., Xu, X., and Zhou, X., 2002, Zircon chemistry and magma mixing, SE China: In-situ analysis of Hf isotopes, Tonglu and Pingtan igneous complexes: Lithos, v. 61, p. 237-269.

Hassan, T., Asran, A., Amron, T., and Hauzenberger, C., 2014, Petrogenesis of selected A-type granitic intrusions from Central Eastern Desert of Egypt: EGUGA, p. 6223.

Henry, B., Liégeois, J.-P., Nouar, O., Derder, M., Bayou, B., Bruguier, O., Ouabadi, A., Belhai, D., Amenna, M., and Hemmi, A., 2009, Repeated granitoid intrusions during the Neoproterozoic along the western boundary of the Saharan metacraton, Eastern Hoggar, Tuareg shield, Algeria: an AMS and U–Pb zircon age study: Tectonophysics, v. 474, no. 3-4, p. 417-434.

Isseini, M., André-Mayer, A.-S., Vanderhaeghe, O., Barbey, P., and Deloule, E., 2012, A-type granites from the Pan-African orogenic belt in south-western Chadconstrained using geochemistry, Sr–Nd isotopes and U–Pb geochronology: Lithos, v. 153, p. 39-52.

Jackson, S. E., Pearson, N. J., Griffin, W. L., and Belousova, E. A., 2004, The application of laser ablation-inductively coupled plasma-mass spectrometry to in-situ U/Pb zircon geochronology: Chemical Geology, v. 211, p. 47-69.

Johnson, P. R., 2014, An Expanding Arabian-Nubian Shield Geochronologic and Isotopic Dataset: Defining Limits and Confirming the Tectonic Setting of a Neoproterozoic Accretionary Orogen: The Open Geology Journal, v. 8, p. 3-33.

Johnson, P. R., Andresen, A., Collins, A. S., Fowler, A. R., Fritz, H., Ghebreab, W., Kusky, T., and Stern, R. J., 2011, Late Cryogenian-Ediacaran history of the Arabian-Nubian Shield: A review of depositional, plutonic, structural, and tectonic events in the closing stages of the northern East African Orogen: Journal of African Earth Sciences, v. 61, no. 3, p. 167-232.

Johnson, P. R., and Woldehaimanot, B., 2003, Development of the Arabian-Nubian Shield: perspectives on accretion and deformation in the northern East African Orogen and the assembly of Gondwana, in Yoshida, M., Windley, B. F., and Dasgupta, S., eds., Proterozoic East Gondwana: Supercontinent Assembly and Breakup, Geological Society, London, Special Publication 206, p. 289-325.

Kennedy, W. Q., 1964, The structural differentiation of Africa in the Pan-African (+/- 500 m.y.) Tectonic Episode, Eighth Annual Report on Scientific Results of the Research Institute of African Geology, University of Leeds., p. 48-49.

Kroner, A., 1977, Precambrian mobile belts of southern and eastern Africa—ancient sutures or sites of ensialic mobility? A case for crustal evolution towards plate tectonics: Tectonophysics, v. 40, no. 1-2, p. 101-135.

Kröner, A., Linnebacher, P., Stern, R., Reischmann, T., Manton, W., and Hussein, I., 1991, Evolution of Pan-African island arc assemblages in the southern Red Sea Hills, Sudan, and in southwestern Arabia as exemplified by geochemistry and geochronology: Precambrian Research, v. 53, no. 1-2, p. 99-118.

Küster, D., and Harms, U., 1998, Post-collisional potassic granitoids from the southern and northwestern parts of the Late Neoproterozoic East African Orogen: a review: Lithos, v. 45, p. 177-195.

Küster, D., and Liégeois, 2001, Sr, Nd isotopes and geochemistry of the Bayuda Desert high-grade metamorphic basement (Sudan): an early Pan-African oceanic convergent margin, not the edge of the East Saharan ghost craton?: Precambrian Research, v. 109, p. 1-23.

Küster, D., Liégeois, J.-P., Matukov, D., Sergeev, S., and Lucassen, F., 2008, Zircon geochronology and Sr, Nd, Pb isotope geochemistry of granitoids from Bayuda Desert and Sabaloka (Sudan): evidence for a Bayudian event (920–900 Ma) preceding the Pan-African orogenic cycle (860–590 Ma) at the eastern boundary of the Saharan Metacraton: Precambrian Research, v. 164, no. 1-2, p. 16-39.

Li, Z. X., Bogdanova, S. V., Collins, A. S., Davidson, A., De Waele, B., Ernst, R. E., Fitzsimons, I. C. W., Fuck, R. A., Gladkochub, D. P., Jacobs, J., Karlstrom, K. E., Lu, S., Natapov, L. M., Pease, V., Pisarevsky, S. A., Thrane, K., and Vernikovsky, V., 2008, Assembly, configuration, and break-up history of Rodinia: A synthesis: Precambrian Research, v. 160, no. 1-2, p. 179-210.

Liégeois, J.-P., Abdelsalam, G., Ennih, N., and Ouabadi, A., 2013, Metacraton: Nature, genesis and behavior: Gondwana Research, v. 23, p. 220-237.

Liégeois, J.-P., Benhallou, A., Azzouni-Sekkal, A., Yahiaoui, R., and Bonin, B., 2005, The Hoggar swell and volcanism, Tuareg shield, Central Sahara: intraplate reactivation of Precambrian structures as a result of Alpine convergence: Plates, Plumes and Paradigms. Geological Society of America Special Paper, v. 388, p. 379-400.

Liégeois, J.-P., Black, R., Navez, J., and Latouche, L., 1994, Early and late Pan-African orogenies in the Air assembly of terranes (Tuareg Shield, Niger): Precambrian research, v. 67, no. 1-2, p. 59-88.

Liegeois, J. P., Latouche, L., Boughrara, M., Navez, J., and Guiraud, M., 2003, The LATEA metacraton (Central Hoggar, Tuareg shield, Algeria): behaviour of an old passive margin during the Pan-African orogeny: Journal of African Earth Sciences, v. 37, no. 3-4, p. 161-190.

Liégeois, J. P., Latouche, L., Boughrara, M., Navez, J., and Guiraud, M., 2003, The LATEA metacraton (Central Hoggar, Tuareg shiled, Algeria): behaviour of an old passive margin during the Pan-African orogeny: Journal of African Earth Sciences, v. 37, p. 161-190.

Ludwig, K., 2008, Isoplot version 4.15: a geochronological toolkit for microsoft Excel: Berkeley Geochronology Center, Special Publication, no. 4.

Lundmark, A. M., Andresen, A., Hassan, M. A., Augland, L. E., and Boghdady, G. Y., 2012, Repeated magmatic pulses in the East African Orogen in the Eastern Desert, Egypt: an old idea supported by new evidence: Gondwana Research, v. 22, no. 1, p. 227-237.

Merdith, A. S., Collins, A. S., Williams, S. E., Pisarevsky, S., Foden, J. D., Archibald, D. B., Blades, M. L., Alessio, B. L., Armistead, S., Plavsa, D., Clark, C., and Muller, R. D., 2017, A full-plate global reconstruction of the Neoproterozoic: Gondwana Research, v. 50, p. 84-134.

Merdith, A. S., Williams, S. E., Collins, A. S., Tetley, M. G., Mulder, J. A., Blades, M. L., Young, A., Armistead, S. E., Cannon, J., Zahirovic, S., and Müller, R. D., 2020, Extending full-plate tectonic models into deep time: Linking the Neoproterozoic and the Phanerozoic: Earth-Science Reviews.

Nkoumbou, C., Barbey, P., Yonta-Ngouné, C., Paquette, J.-L., and Villiéras, F., 2014, Pre-collisional geodynamic context of the southern margin of the Pan-African fold belt in Cameroon: Journal of African Earth Sciences, v. 99, p. 245-260.

Owona, S., Ondoa, J. M., Ratschbacher, L., Ndzana, S. P. M., Tchoua, F. M., and Ekodeck, G. E., 2011, The geometry of the Archean, Paleo-and Neoproterozoic tectonics in the Southwest Cameroon: Comptes Rendus Geoscience, v. 343, no. 4, p. 312-322.

Paquette, J., Caby, R., Djouadi, M., and Bouchez, J., 1998, U–Pb dating of the end of the Pan-African orogeny in the Tuareg shield: the post-collisional syn-shear Tioueine pluton (Western Hoggar, Algeria): Lithos, v. 45, no. 1-4, p. 245-253.

Payne, J. L., Pearson, N. J., Grant, K. J., and Halverson, G. P., 2013, Reassessment of relative oxide formation rates and molecular interferences on in situ lutetium-hafnium analysis with laser ablation MC-ICP-MS: Journal of Analytical Atomic Spectrometry, v. 28, no. 7, p. 1068-1079.

Penaye, J., Kröner, A., Toteu, S. F., Van Schmus, W. R., and Doumnang, J.-C., 2006, Evolution of the Mayo Kebbi region as revealed by zircon dating: an early (ca. 740 Ma) Pan-African magmatic arc in southwestern Chad: Journal of African Earth Sciences, v. 44, no. 4-5, p. 530-542.

Peucat, J. J., Drareni, A., Latouche, L., Deloule, E., and Vidal, P., 2003, U-Pb zircon (TIMS and SIMS) and Sm-Nd whole-rock geochronology of the Gour Oumelalen granulitic basement, Hoggar massif, Tuareg shield, Algeria: Journal of African Earth Sciences, v. 37, no. 3-4, p. 229-239.

Pin, C., and Poidevin, J., 1987, U-Pb zircon evidence for a Pan-African granulite facies metamorphism in the Central African Republic. A new interpretation of the high-grade series of the northern border of the Congo Craton: Precambrian Research, v. 36, no. 3-4, p. 303-312.

Pisarevsky, S. A., Murphy, J. B., Cawood, P. A., and Collins, A. S., 2008, Late Neoproterozoic and Early Cambrian palaeogeography: models and problems, *in* Brito Neves, B. B., Trouw, R. A. J., de Wit, M. J., and Pankhurst, R. J., eds., Western Gondwana: Pre-Cenozoic Geology Bordering the South Atlantic, Volume 294, Geological Society, London, Special Publication, p. 9-32.

Robinson, F. A., Bonin, B., Pease, V., and Anderson, J. L., 2017, A discussion on the tectonic implications of Ediacaran late- to post-orogenic A-type granite in the northeastern Arabian Shield, Saudi Arabia: Tectonics, v. 36, no. 3, p. 582-600.

Robinson, F. A., Foden, J. D., and Collins, A. S., 2015a, Geochemical and isotopic constraints on island arc, synorogenic, post-orogenic and anorogenic granitoids in the Arabian Shield, Saudi Arabia: Lithos, v. 220, p. 97-115.

-, 2015b, Zircon Geochemical and Geochronological Constraints on Contaminated and Enriched Mantle Sources beneath the Arabian Shield, Saudi Arabia: Journal of Geology, v. 123, no. 5, p. 463-489.

Robinson, F. A., Foden, J. D., Collins, A. S., and Payne, J. L., 2014, Arabian Shield magmatic cycles and their relationship with Gondwana assembly: Insights from zircon U-Pb and Hf isotopes: Earth and Planetary Science Letters, v. 408, p. 207-225.

Schandelmeier, H., Huth, A., Harms, U., Franz, G., and Bernau, R., 1987, The East Sahara Craton in Southern Egypt and Northern Sudan: lithology, metamorphism, magmatism, geochronology and structural development.

Schandelmeier, H., Rahman, E. A., Wipfler, E., Küster, D., Utke, A., and Matheis, G., 1994, Late Proterozoic magmatism in the Nakasib suture, Red Sea Hills, Sudan: Journal of the Geological Society, v. 151, no. 3, p. 485-497.

Scherer, E., Münker, C., and Mezger, K., 2001, Calibration of the lutetium-hafnium clock: Science, v. 293, p. 683-687.

Schneider, J., and Wolf, J., 1992, Geological map and hydrogeological maps on scale 1/500,000 of Chad Republic. Explanatory project document of BRGM.

Şengör, A. M. C., Lom, N., Zabcı, C., Sunal, G., and Öner, T., 2020, Reconstructing orogens without biostratigraphy: The Saharides and continental growth during the final assembly of Gondwana-Land: Proceedings of the National Academy of Sciences, v. 117, no. 51, p. 32278-32284.

Shackleton, R., 1996, The final collision zone between East and West Gondwana: where is it?: Journal of African Earth Sciences, v. 23, no. 3, p. 271-287.

Shalaby, A., Stüwe, K., Makroum, F., Fritz, H., Kebede, T., and Klötzli, U., 2005, The Wadi Mubarak belt, Eastern Desert of Egypt: a Neoproterozoic conjugate shear system in the Arabian–Nubian Shield: Precambrian Research, v. 136, no. 1, p. 27-50.

Shellnutt, J. G., Pham, N. H. T., Denyszyn, S. W., Yeh, M.-W., and Lee, T.-Y., 2017, Timing of collisional and post-collisional Pan-African Orogeny silicic magmatism in south-central Chad: Precambrian Research, v. 301, p. 113-123.

Shellnutt, J. G., Pham, N. H. T., Yeh, M.-W., and Lee, T.-Y., 2020, Two series of Ediacaran collision-related granites in the Guéra Massif, South-Central Chad: Tectonomagmatic constraints on the terminal collision of theeastern Central African Orogenic Belt: Precambrian Research, v. 347, p. 105823.

Shellnutt, J. G., Yeh, M.-W., Lee, T.-Y., Iizuka, Y., Pham, N. H. T., and Yang, C.-C., 2018, The origin of Late Ediacaran post-collisional granites near the Chad Lineament, Saharan Metacraton, south-central Chad: Lithos, v. 304, p. 450-467.

Sláma, J., Kosler, J., Condon, D. J., Crowley, J. L., Gerdes, A., Hanchar, J. M., Horstwood, M. S. A., Morris, G. A., Nasdala, L., Norberg, N., Schaltegger, U., Schoene, B., Tubrett, M. N., and Whitehouse,

M. J., 2008, Plesovice zircon - A new natural reference material for U-Pb and Hf isotopic microanalysis.: Chemical Geology, v. 249, p. 1-35.

Stern, R. A., 2002, Crustal evolution in the East African Orogen: a neodymian isotopic perspective: Journal Of African Earth Sciences, v. 34, p. 109-117.

Stern, R. A., and Hedge, C. E., 1985, Geochronologic and isotopic constraints on Late Precambrian crustal evolution in the Eastern Desert of Egypt: American Journal of Science, v. 285, p. 97-127.

Stern, R. J., 1994, Arc Assembly and continental collision in the Neoproterozoic East African orogeny - implications for the consolidation of Gondwana: Annual Review of Earth and Planetary Sciences, v. 22, p. 319-351.

Stoeser, D., and Stacey, J., Evolution, U-Pb geochronology, and isotope geology of the Pan-African Nabitah orogenic belt of the Saudi Arabian Shield, in Proceedings The Pan-African belt of Northeast Africa and adjacent areas: tectonic evolution and economic aspects of a late proterozoic oregon1988, p. 227-288.

Stoeser, D. B., Whitehouse, M. J., and Stacey, J. S., 2001, The Khida Terrane -- Geology of Paleoproterozoic Rocks in the Muhayil Area, Eastern Arabian Shield, Saudi Arabia: Gondwana Research, v. 4, no. 2, p. 192-194.

Suayah, I. B., Miller, J. S., Miller, B. V., Bayer, T. M., and Rogers, J. J., 2006, Tectonic significance of Late Neoproterozoic granites from the Tibesti massif in southern Libya inferred from Sr and Nd isotopes and U–Pb zircon data: Journal of African Earth Sciences, v. 44, no. 4-5, p. 561-570.

Sultan, M., Tucker, R., El Alfy, Z., Attia, R., and Ragab, A. G., 1994, U-Pb (zircon) ages for the gneissic terrane west of the Nile, southern Egypt: Geologische Rundschau, v. 83, no. 3, p. 514-522.

Tang, M., Wang, X. L., Shu, X. J., Wang, D., Yang, T., and Gopon, P., 2014, Hafnium isotopic heterogeneity in zircons from granitic rocks: Geochemical evaluation and modeling of "zircon effect" in crustal anatexis: Earth and Planetary Science Letters, v. 389, p. 188-199.

Tchakounté, J., Eglinger, A., Toteu, S. F., Zeh, A., Nkoumbou, C., Mvondo-Ondoa, J., Penaye, J., de Wit, M., and Barbey, P., 2017, The Adamawa-Yadé domain, a piece of Archaean crust in the Neoproterozoic Central African Orogenic belt (Bafia area, Cameroon): Precambrian Research, v. 299, p. 210-229.

Teklay, M., Haile, T., Kröner, A., Asmerom, Y., and Watson, J., 2003, A back-arc palaeotectonic setting for the Augaro Neoproterozoic magmatic rocks of western Eritrea: Gondwana Research, v. 6, no. 4, p. 629-640.

Toteu, S., Michard, A., Bertrand, J., and Rocci, G., 1987, U/Pb dating of Precambrian rocks from Northern Cameroon, orogenic evolution and chronology of the Pan-African belt of Central Africa: Precambrian Research, v. 37, no. 1, p. 71-87.

Toteu, S., Penaye, J., RANDY VAN SCHMUS, W., and Michard, A., 1994, Preliminary U-Pb and Sm-Nd geochronologic data on the North-Central Cameroon: contribution of an Archean and paleo-Proterozoic crust to the edification of an active domain of the Pan-African orogeny: Comptes rendus de l'Académie des sciences. Série 2. Sciences de la terre et des planètes, v. 319, no. 12, p. 1519-1524.

Toteu, S. F., Penaye, J., Deloule, E., Van Schmus, W. R., and Tchameni, R., 2006, Diachronous evolution of volcano-sedimentary basins north of the Congo craton: Insights from U-Pb ion microprobe dating of zircons from the Poli, Lom and Yaounde Groups (Cameroon): Journal of African Earth Sciences, v. 44, no. 4-5, p. 428-442.

Toteu, S. F., Penaye, J., and Djomani, Y. P., 2004, Geodynamic evolution of the Pan-African belt in central Africa with special reference to Cameroon: Canadian Journal of Earth Science, v. 41, p. 73-85.

Toteu, S. F., Van Schmus, W. R., Penaye, J., and Michard, A., 2001, New U-Pb and Sm-Nd data from north-central Cameroon and its bearing on the pre-Pan African history of central Africa: Precambrian Research, v. 108, no. 1-2, p. 45-73.

Vail, P. R., 1983, Seismic Stratigraphy and the Evaluation of Depositional Sequences and Facies: Geophysical Journal of the Royal Astronomical Society, v. 73, no. 1, p. 278-278.

Van Achterbergh, E., Ryan, C. G., Jackson, S. E., and Griffin, W. L., 2001, Data reduction software for LA-ICP-MS, in Sylvester, P. J., ed., Laser-ablation-ICPMS in the earth sciences; principles and

applications, Volume 29: Ottowa, Mineralogical Association of Canada, Short Course Handbook, p. 239-243.

Vicat, J. P., Moloto-A-Kenguemba, G., and Pouclet, A., 2001, Granitoids of the Proterozoic cover of the Congo craton northern edge (South-East of Cameroon and South-West of the Central African Republic), witnesses of a post-Kibarian to pre-Pan-African magmatic activity: Comptes Rendus De L Academie Des Sciences Serie Ii Fascicule a-Sciences De La Terre Et Des Planetes, v. 332, no. 4, p. 235-242.

Whitehouse, M. J., Stoeser, D. B., and Stacey, J. S., 2001, The Khida Terrane -- Geochronological and Isotopic Evidence for Paleoproterozoic and Archean Crust in the Eastern Arabian Shield of Saudi Arabia: Gondwana Research, v. 4, no. 2, p. 200-202.

Woodhead, J. D., Hergt, J. M., Shelley, M., Eggins, S., and Kemp, R., 2004, Zircon Hf-isotope analysis with an Excimer laser, depth profiling, ablation of complex geometries, and concomitant age estimation.: Chemical Geology, v. 209, p. 121-135.

Yeshanew, F. G., Pease, V., Abdelsalam, M. G., and Whitehouse, M. J., 2017, Zircon U-Pb ages, delta O-18 and whole-rock Nd isotopic compositions of the Dire Dawa Precambrian basement, eastern Ethiopia: implications for the assembly of Gondwana: Journal of the Geological Society, v. 174, no. 1, p. 142-156.
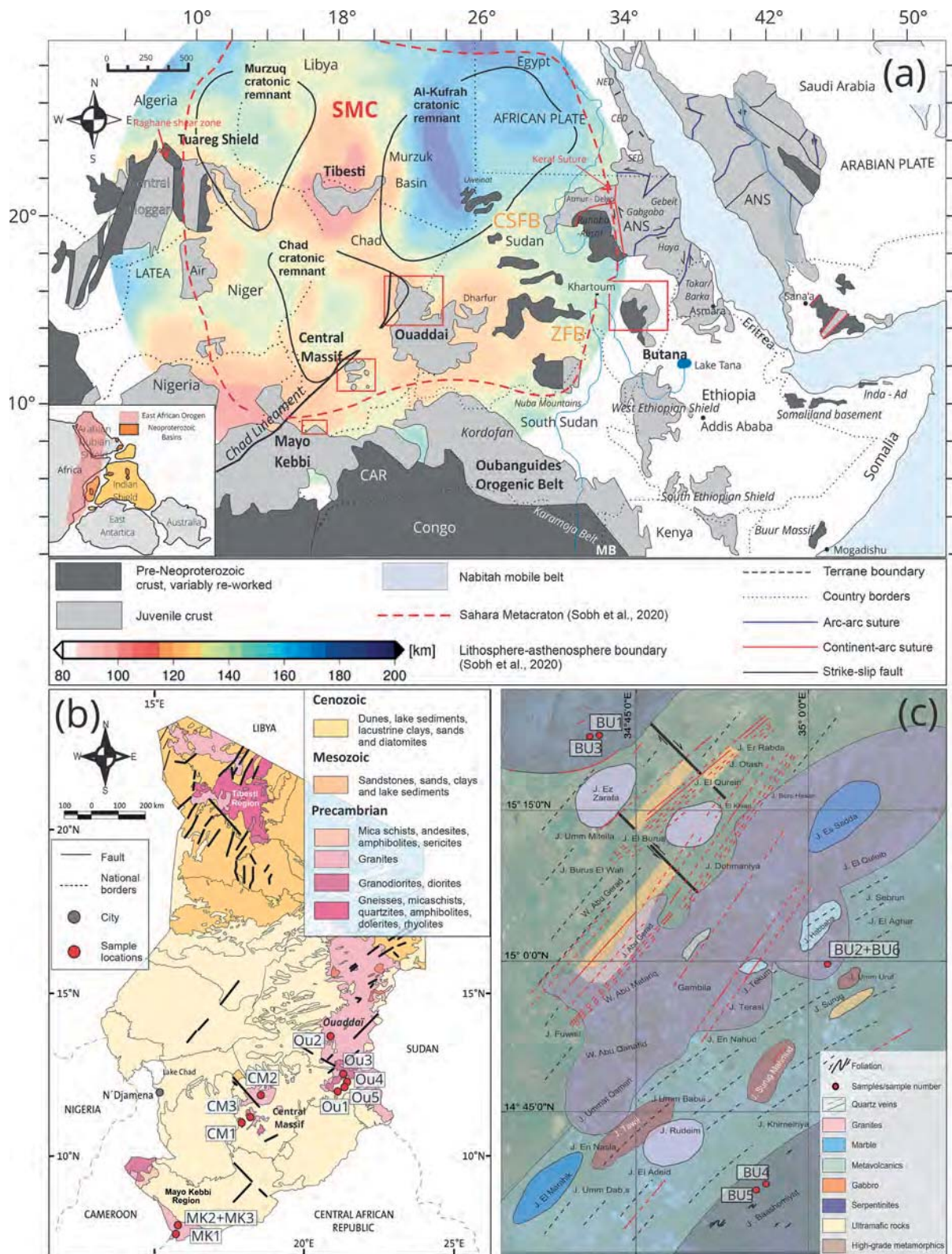
Fig. 1. a) Location map of the Saharan Metacraton (SMC) and the Arabian Nubian Shield (ANS) (adapted from Blades et al., 2015; Johnson et al., 2014 and Abdelsalam et al. 2002). Red boxes indicate the regions of Mesoproterozoic and Neoproterozoic basement sampled in this study. The previously suggested extents of Sahara Metacraton outlined based on geophysical data by Sobh et al. (2020) are also shown. The geophysical data indicate preservation of three cratonic remnants (Murzuq, Al-Kufrah and Chad) within the Sahara Metacraton. A representation of lithosphere-asthenosphere boundary underneath the Sahara Metacraton is included with the colour gradation (taken from Sobh et al., 2020). The location of the Chad Lineament is taken from Shellnutt et al. (2018). CSFB = Central Saharan Fold Felt, ZFB = Zalingai Fold Belt (de Wit and Linol, 2015). b) Geological map of Chad, showing the samples collected from the Precambrian exposures. Taken from and modified after Saleh (1994) and Schluter (2008). c) First geological map of Butana constructed by Abu-Alam., T.S. and presented in this manuscript. (For interpretation of the references to colour in this figure legend, the reader is referred to the web version of this article.)
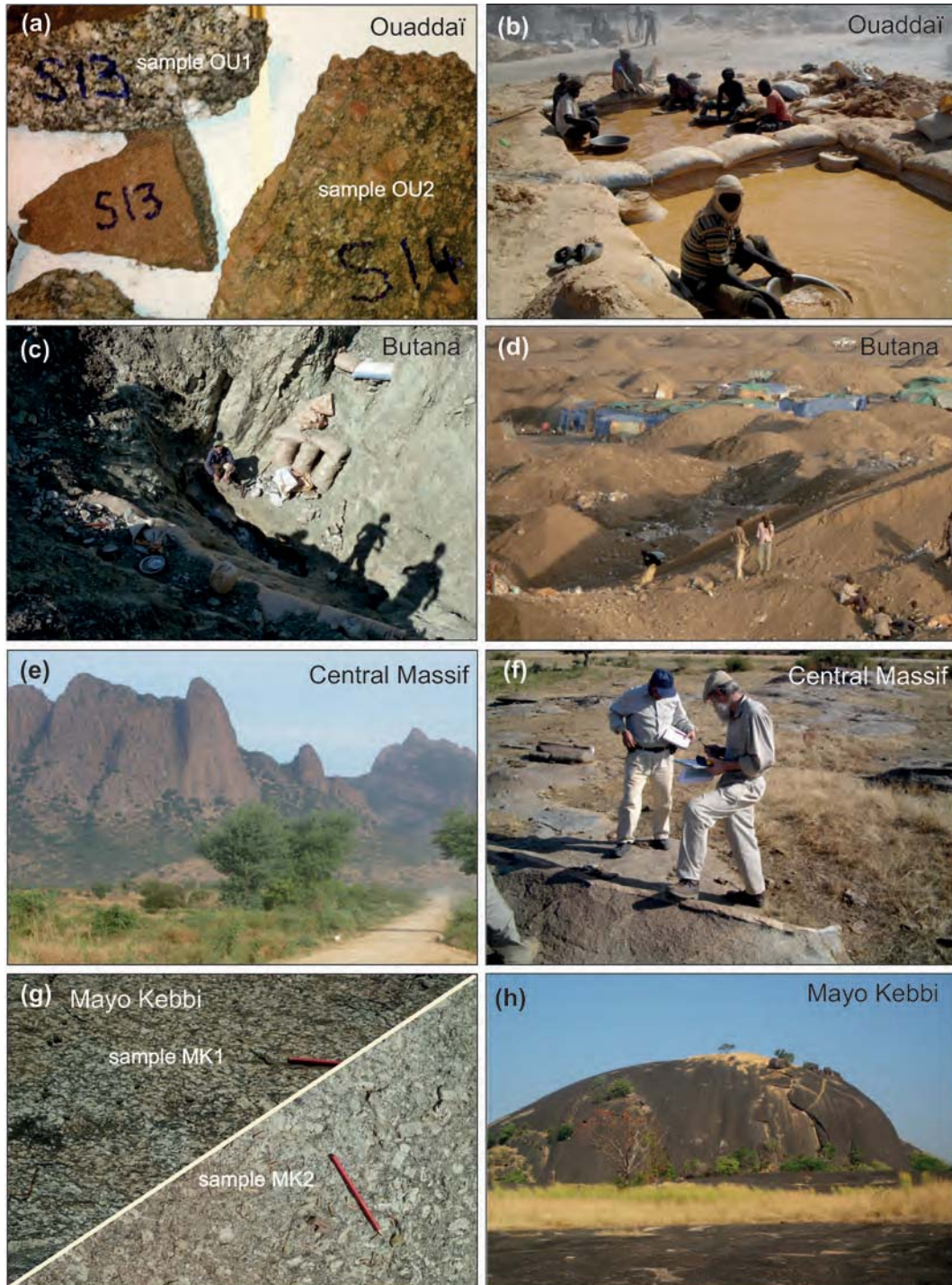
Fig. 2. Field photographs of the sample locations discussed in this paper. (a) Close up view of the monzogranite samples from the Ouaddaï region (b) Artisan gold mining is wide spread in the Ouaddaï region. (c) The Butana region is largely covered by allochthonous sediment plains and outcrops are almost exclusively in man-made outcrops of artisan gold mines. (d) Major gold mining operation in the Butana region. (e) Granite peaks in the Central Massif of Chad. (f) Sample location of sample CM1 in the Central Massif of Chad. (g) Field photographs of samples MK1 and MK2. (h) Typical field occurrence of granitic hills in the Mayo Kebbi region of southern Chad.
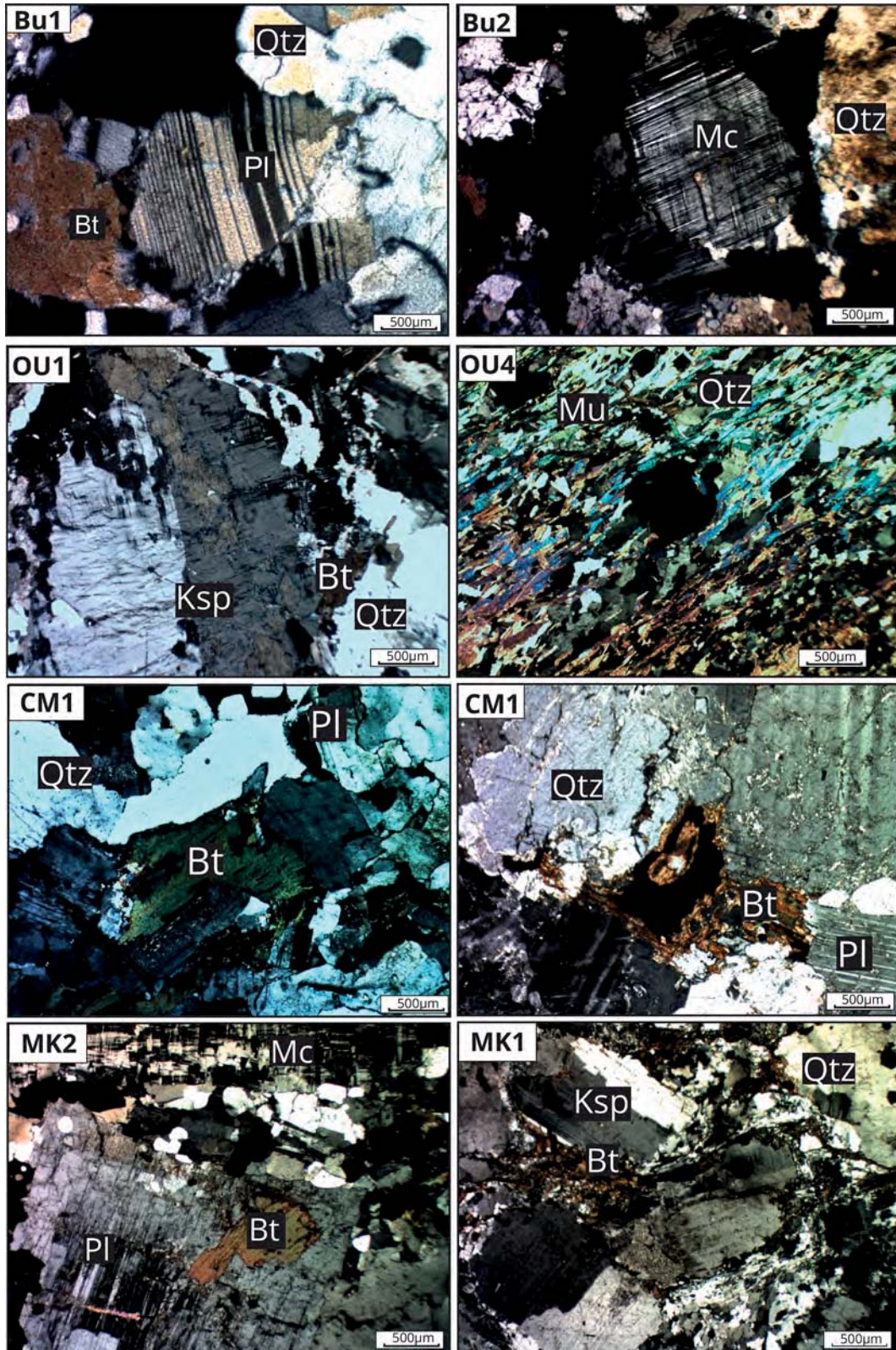
Fig. 3. Thin section images of the igneous samples collected from Chad and Sudan, in cross polarised light. Minerals present are labelled where. Qtz is quartz; Bt is biotite; Pl is plagioclase; Mc is microcline and Ksp is K-feldspar.

Fig. 4. Representative CL images for all (meta)igneous rocks sampled in Chad and Sudan. U–Pb laser (yellow) and Hf (orange) spots shown. The zircons from Butana are generally fragmented, or rounded. Grains have faint oscillatory zonation or sector zoning, though in places original textures have been replaced by homogeneous lobes and patches. Some grains preserve ghost/ remnants of previous zoning and some have no definable features. The zircons from Chad have faint oscillatory zonation or sector zoning, with darker rims mantling some grains. There are strong variations in the relative development of zoned domains, where one large uniform central zone is succeeded by much finer oscillatory-zoned bands. Spot numbers refer to analyses in Supplementary Table 1.
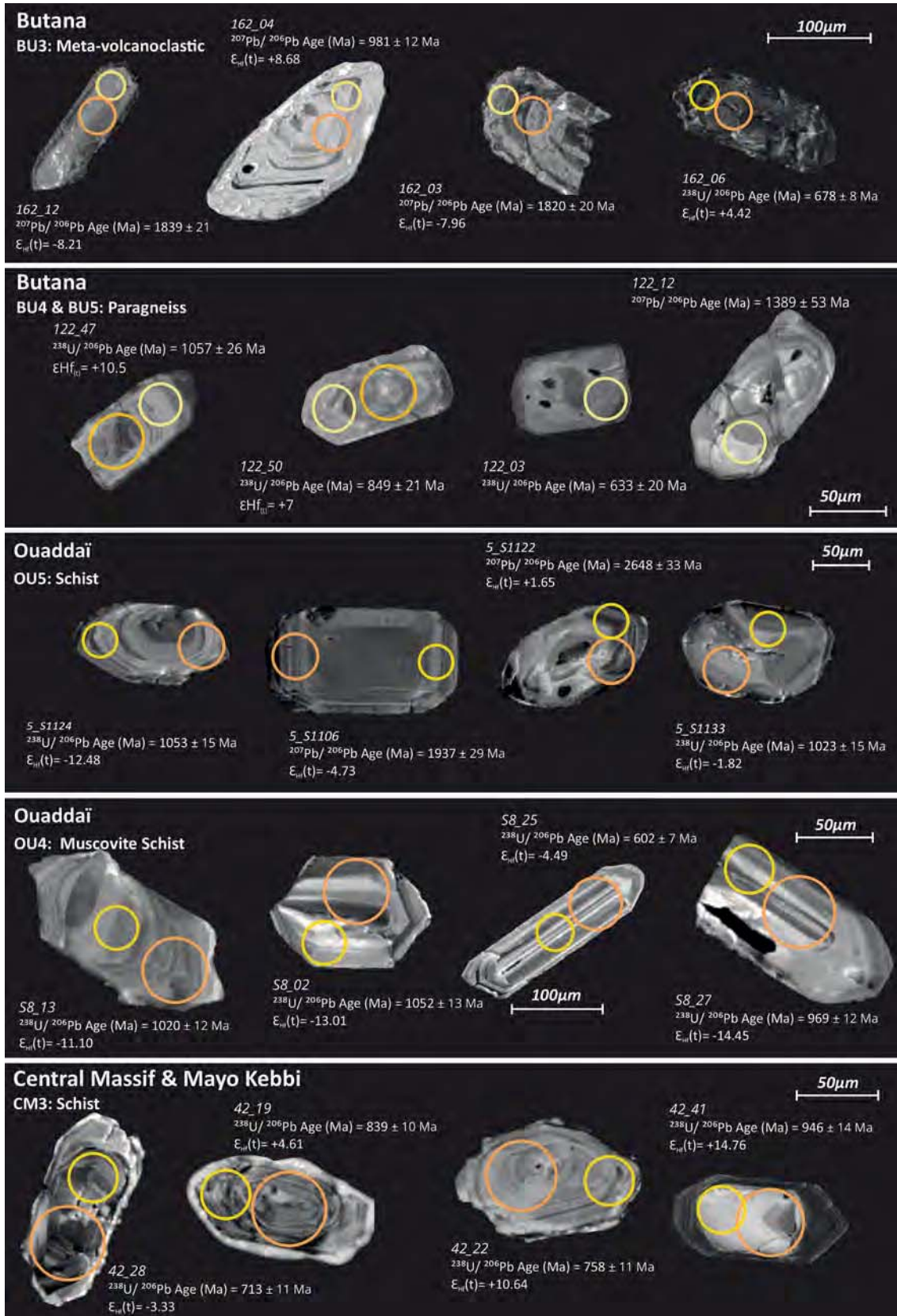
Fig. 5. Representative CL images for all metasedimentary rocks sampled in Chad and Sudan. Grains were selected to represent age populations within the samples. U–Pb laser (yellow) and Hf (orange) spots are shown on the grains. Spot numbers refer to analyses in Supplementary Table 1.
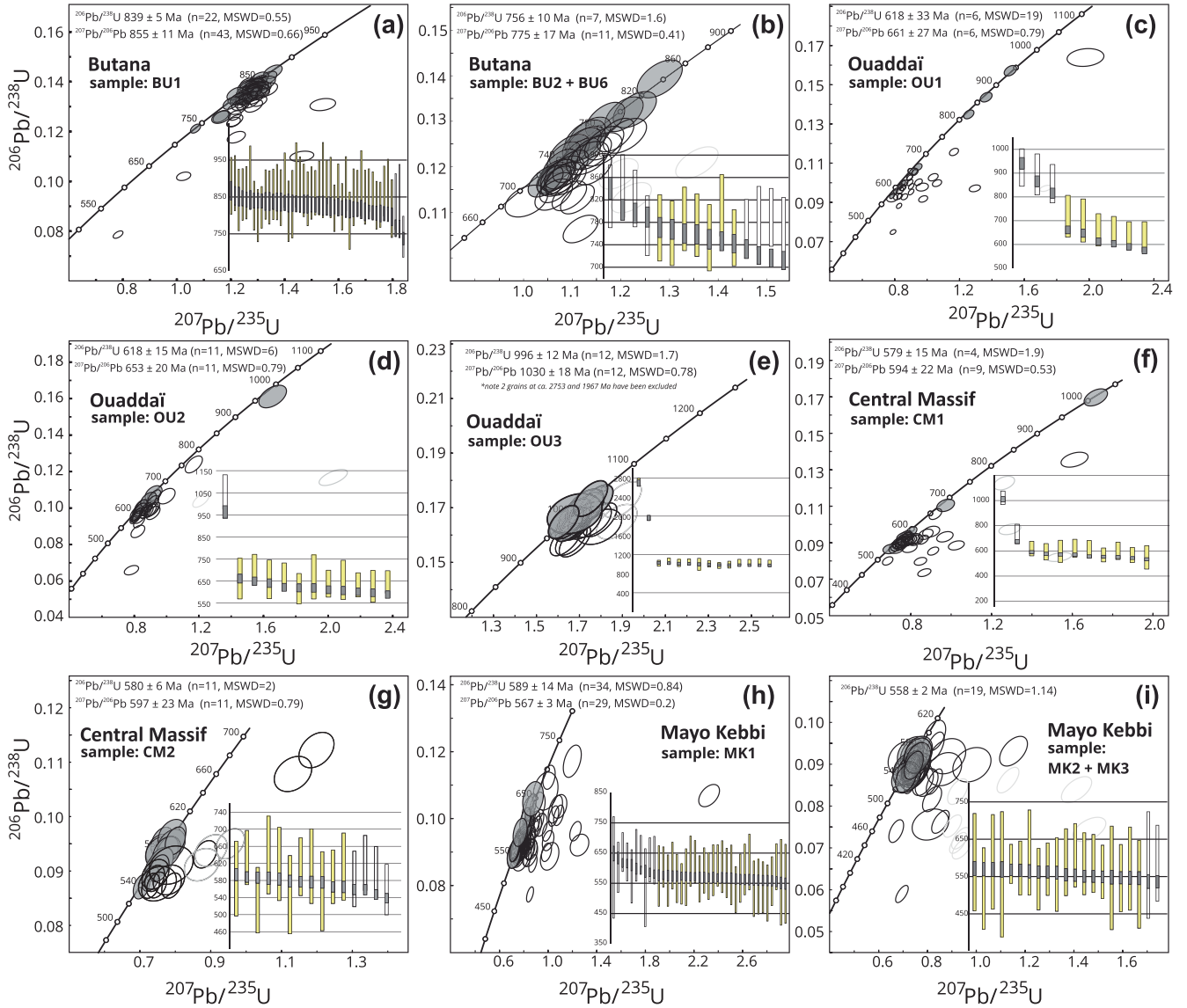
Fig. 6. U–Pb Wetherill plots (^{207}Pb/^{206}Pb v. ^{238}U/^{206}Pb) for each igneous sample from Butana and Chad, samples are labelled. These plots are constructed with a 2σ data point error ellipses, analyses within ≥ 90% concordance are shown in grey and those that fall outside this range are non-filled ellipses. Weighted average plots for all igneous samples are shown in each concordia. Grey bars are ^{206}Pb/^{238}U ages with 2σ errors. Yellow bars represent the ^{207}Pb/^{206}Pb ages with 2σ errors. These plots are used to highlight any trends in the data. (For interpretation of the references to colour in this figure legend, the reader is referred to the web version of this article.)
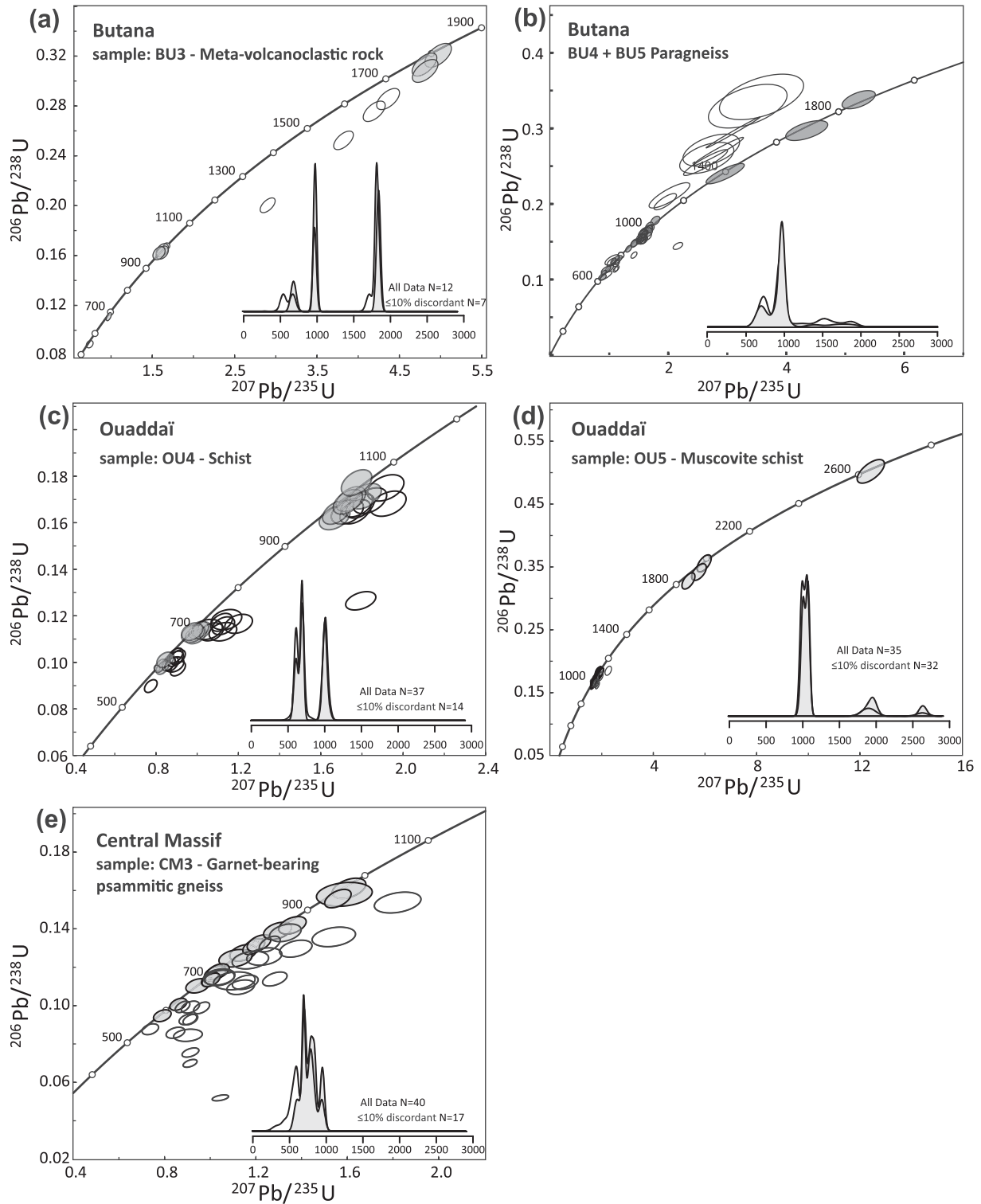
Fig. 7. U–Pb Wetherill plots (^{207}Pb / ^{206}Pb v. ^{238}U/^{206}Pb) and kernel density estimate plots for metasedimentary samples from Butana and Chad. These are 2σ data point ellipses. The kernel density estimate plots only contain data that are concordant to ≥ 90%. The filled ellipses denote analyses that are concordant to ≥ 90%. Unfilled ellipses are those that fall outside this range.
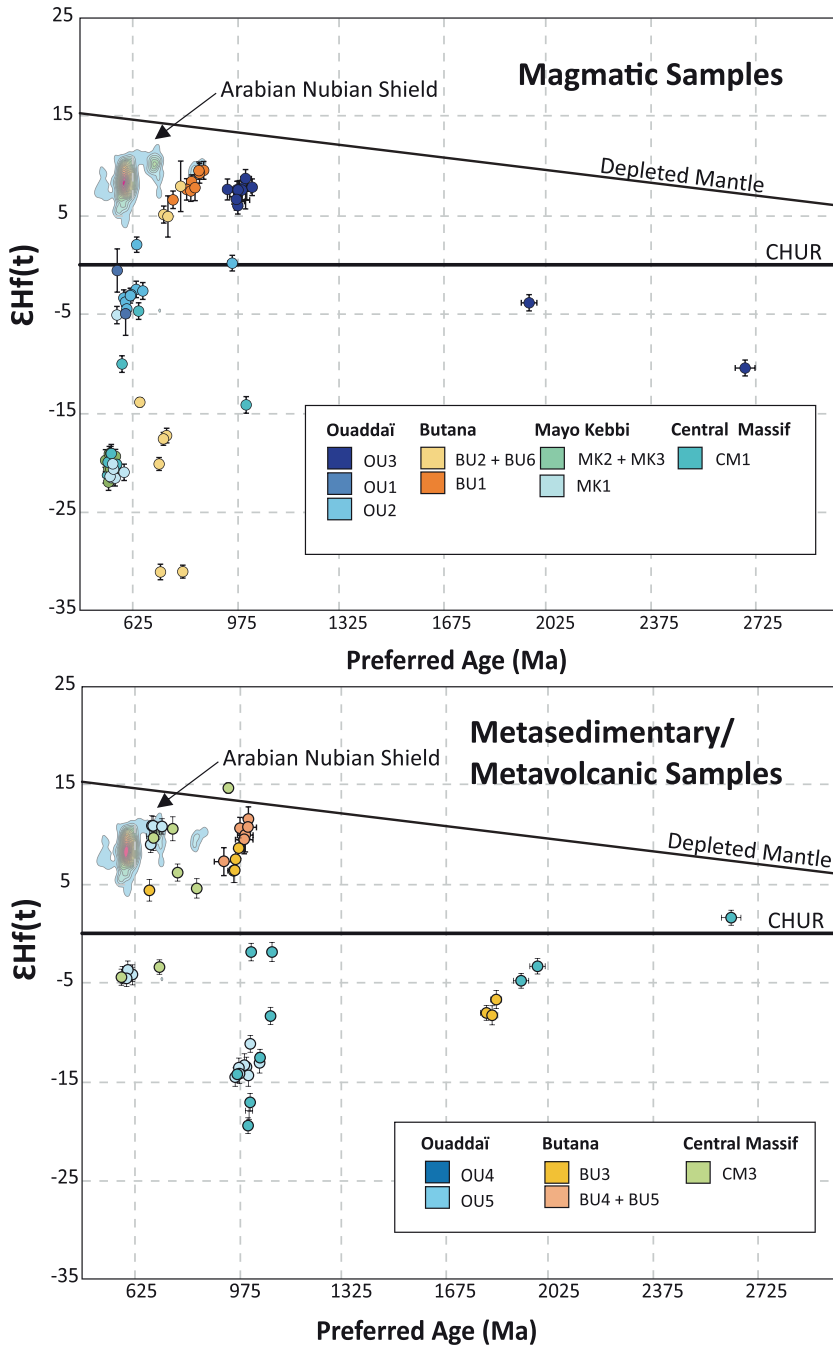
Fig. 8. a) $\bar{A}_{Hf}$ (t) versus preferred age (Ma) plot for all igneous samples from Butana and Chad. Butana hafnium isotopic values suggest juvenile magmatism ($\bar{A}_{Hf}$(t) of +4.89 to +7.89). The Cryogenian and Ediacaran magmatism within the Sahara Metacraton have $\bar{A}_{Hf}$(t) values between +2.04 and −4.07. Both horizontal and vertical error bars show 2σ error. b) $\bar{A}_{Hf}$ (t) versus preferred age plot for all sedimentary samples. On both figures, previously published data collated from the Arabian Nubian Shield are shown for comparison. These are gridded based on point density, with red suggesting the highest concentration of data points (Alessio et al., 2018; Ali et al., 2013; Ali et al., 2016; Be'eri-Shlevin et al., 2010; Blades et al., 2015; Robinson et al., 2014; Robinson et al., 2015b). (For interpretation of the references to colour in this figure legend, the reader is referred to the web version of this article.)

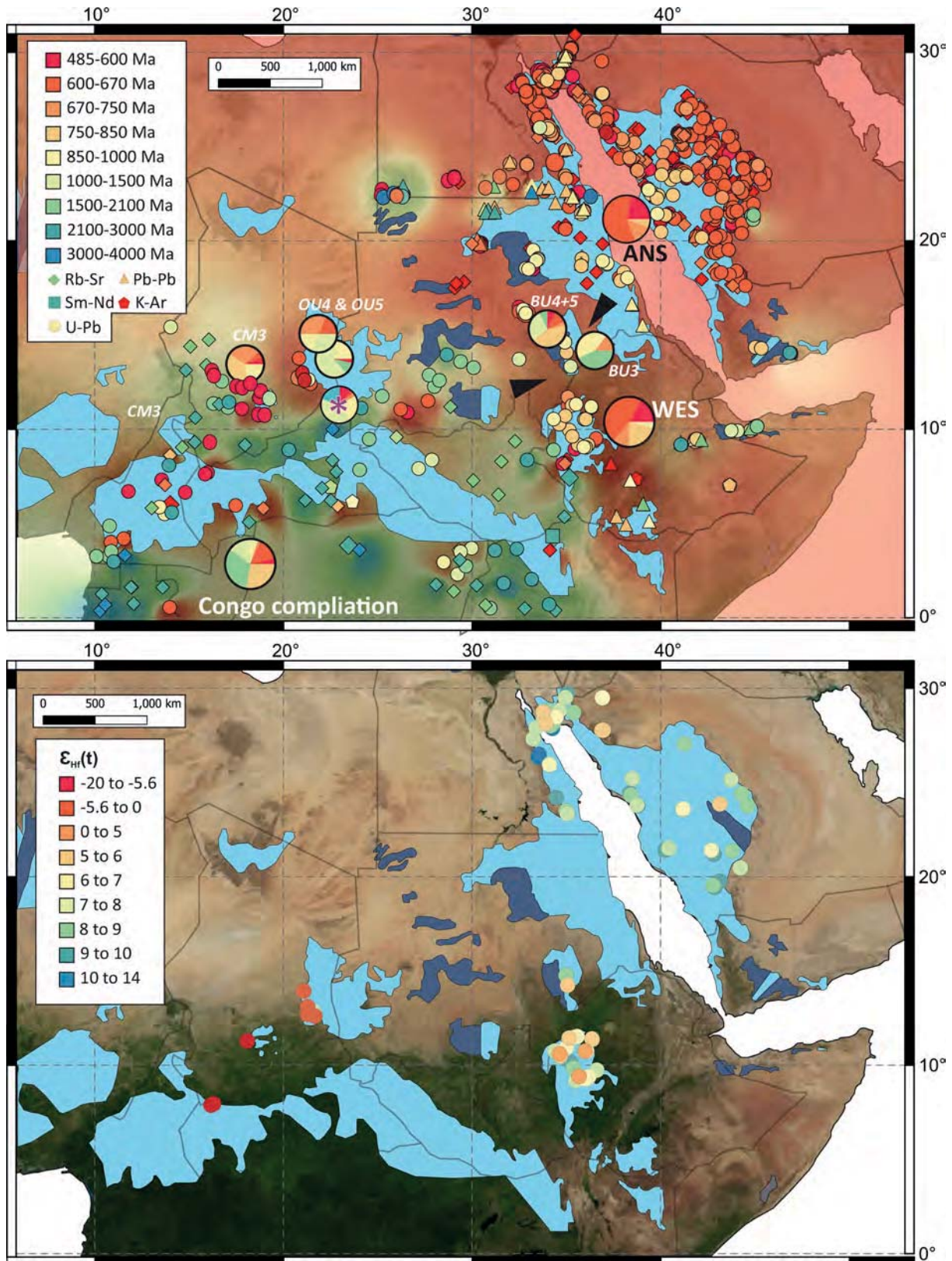**Fig. 9.** a) Collation of all available age data from northern Africa. Data have been divided into different methods, indicated on the legend. Data clearly differentiates the Arabian Nubian Shield from the older mobilised Sahara Metacraton. It is clear that the Sahara Metacraton has a complicated history with multiple phases of magmatism occurring during the Mesoproterozoic and Neoproterozoic, though there is sparse data available from these regions. This map hap has been gridded using QGIS nearest neighbour interpolation, with set age bins to act as a visual aid for the relative distribution of ages in northern Africa (Abdelsalam et al., 2002; Abdelsalam et al., 2003; Abdelsalam et al., 2011; Be'eri-Shlevin et al., 2012; Couzinié et al., 2020; de Wit and Linol, 2015; Djerossem et al. 2020; Djerossem et al., 2021; Henry et al., 2009; Johnson et al., 2011; Johnson, 2014; Küster et al., 2008; Robinson et al., 2014; Robinson et al.,2015a; Robinson et al.,2015b; Robinson et al.,2017; Shellnutt et al. 2017; Shellnutt et al., 2020; Whitehouse et al., 1998; Whitehouse et al., 2001b; Windley et al., 1996; Yeshanew et al., 2015; Yeshanew et al., 2017; Zhang et al. 2019a; Zhang et al., 2019b). The pie charts show the distribution of detrital zircon U–Pb ages in the metasedimentary samples—all samples from this study, except the purple asterisks, which are data from Djerossem et al. 2021. b) Previously published ε_{Hf} (t) values (Alessio et al., 2018; Ali et al., 2013; Ali et al., 2016; Be'eri-Shlevin et al., 2010; Blades et al., 2015; Djerossem et al., 2021; Robinson et al., 2014; Robinson et al., 2015b) have been collated with data from this study and are coloured by selected bins, shown in the legend. Data highlights the juvenile nature of the Arabian Nubian Shield and that the Sahara Metacraton received pulses of juvenile magmatism. This suggests that these are simply not just remelting older crust of the Sahara metacraton. Adapted from Blades et al. (2015). (For interpretation of the references to colour in this figure legend, the reader is referred to the web version of this article.)

Table 1
Summary of (meta)igneous samples, including mineralogy and zircon texture.

Sample	GPS Coordinates		Area	Rock Type	Minerology	Zircon Textures
BU-1	14°37′N	34°56′E	Butana	Monogranite	Qz + Ksp + Pl + Bt. Oxide and Chl. Accessory: Oxide, Ep, Zr	Colour: Size: 70–100 μm Aspect Ratio: Dominant aspect ratio of 7:1 and 3:1. Morphologies and textures: Grain forms are hard to define, grains are rounded and very damaged. Grains have been recrystallised and preserve transgressive recystallisation fronts that replace any pre-exisiting zontation. Some preserve ghost textures in the form of faint osillatory zonation. Fine CL - bright rims mantle the grains.
BU2 + BU6	14°5′N	35°01′E	Butana	Syenogranite	Megacrysts of Mc, Perthite, Qz, Pl and Bt	**Colour:** **Size:** 100–200 μm **Aspect Ratio:** Dominant aspect ratio of 7:2 and 1:1. **Morphologies and textures:** Dominated by {1 0 1} forms. Rounded grains as well as pryamidal grains present. Very cracked grains, that only preserve faint osillatory zonation or sector zoning. Convolute and disjointed boundaries between textures. Recrystallisation fronts give rise to areas of homogeneously textured zircon that replace pre-exisiting textures.
OU1	12°25′N	21°26′E	Darsila	Coarse-grained syenogranite	Qz + Mc + Pl + Bt, Sphene and Oxides are accessories. Deformed and partially altered.	**Colour:** Size: 60–150 μm Aspect Ratio: Dominant aspect ratio of 4:3, 7:1 and 2:1. **Morphologies and textures:** Dominated by {1 0 0} and {1 0 1} forms. Grains can be divided into two groups. Elongate pyramidal grains some with well defined zonation, a few are homogeneous, with no definable features. Group 2 - rounded grains, with both osillatory and pachy zonation. Convolute and disjointed boundaries exist between textures in both groups. Dark rims are seen mantling a homogeneous core. Recrystallisation fronts seen in grains from both groups.
OU2	13°46′N	20°50′E	Darsila	Coarse-grained syenogranite	Qz + Mc + Pl + Bt, Sphene and Oxides are accessories. Deformed and partially altered.	**Colour:** Size: 150–300 μm Aspect Ratio: Dominant aspect ratio of 4:1, 3:1 and 2:1. **Morphologies and textures:** Dominated by {1 1 0} and {1 0 1} forms. Grains have faint osillatory zonation, which is either convolute or disjointed boundaries between textures. Areas of homogeneously textured zircon appearing as transgressive (across all pre-existing textures) zircon patches and lobes. Defined thin rims mantling some grains. Relative development of zoned domains vary, where one large uniform central zone is succeeded by much finer oscillatory-zoned bands. Some grains are cracked/fragmented and preserve metamict textures.
OU3	12°38′N	21°20′E	Darsila	Orthogneiss	Well foliated Ms with Qz , Pl, Oxides. Crd.	**Colour:** Size: 100–200 μm Aspect Ratio: Dominant aspect ratio of 4:3, 2:1 and 1:1 **Morphologies and textures:** 2 main groups of zircons. Group 1 is definted by {1 0 0} and {1 1 0} forms. Some grains have well developed osillatory zonation. The relative development in zonation varies accross the group. Group 2 is defined by rounded grains. Oscillatory and pachy zonation exists in all. In both groups areas of homogeneously textured zircon appearing as transgressive (across all pre-existing textures) zircon patches and lobes. Fragments of homogeneous zircon are present.
MK1	7°38′N	15°51′E	Chad	Mylonitized granite	Coarse grained perthitic K-spar and plag in fine to medium grained Qz. Well foliated Bt and fine grained Hbl. Zr, Ap and oxides are accessories. Ep present	**Colour:** Pale orange - orange Size: 200–350 μm Aspect Ratio: Majority is 7:2 and 7:1, with some 3:2 and 2:1. **Morphologies and textures:** Dominated by {1 0 1} and {2 1 1} forms. Large cracks present and many are fragmented. Grains have faint osillatory zonation or sector zoning. Convolute boundaries and metamict textures are seen. Areas of homogeneously textured zircon appearing as transgressive (across all pre-existing textures) zircon patches and lobes. Areas of recrystallization occur dominantly at crystal terminations.
MK2 + MK3	7°42′N	15°59′E	Chad	Monzogranite	Mc, K-Spar in medium grained Qz, Plag, Bt and Oxides	**Colour:** Pale orange - orange Size: 250–300 μm Aspect Ratio: Majority is 7:1 and 7:2, with some 3:1. **Morphologies and textures:** Dominated by {1 0 1} and {1 0 0} forms. Large cracks present and many are fragmented. Grains have faint osillatory zonation or sector

Table 1 (*continued*)

Sample	GPS Coordinates		Area	Rock Type	Minerology	Zircon Textures
CM1	11°05′N	17°48′E	Chad	Monzogranite	Qz , Perthite, Mc, K-spar, Pl. Bt (chloritised). Brittle	zoning, with darker rims mantling some grains. There are strong variations in the relative development of zoned domains, where one large uniform central zone is succeeded by much finer oscillatory-zoned bands. **Colour: Size:** 150–200 μm **Aspect Ratio:** Dominant aspect ratio of 5:1 and 2:1. **Morphologies and textures:** Dominated by {1 0 1} pyramidal crystal forms. Crystal terminations have been rounded and grains are cracked. Xenocrystic cores differentiated from their rims by irregular surfaces that truncate internal zoning. Grains have faint oscillatory zonation or sector zoning. Areas of homogeneously textured zircon appearing as transgressive (across all pre-existing textures) zircon patches and lobes.
CM2	12°10′N	18°40′E	Chad	Syenogranite	Megacrysts of perthicic K-spar in medium grained Qz and Pl. 10% Bt (highly chloritised). Oxides are present	**Colour: Size:** 100–200 μm **Aspect Ratio:** Dominant aspect ratio of 7:1 and 3:1. **Morphologies and textures:** Dominated by {1 0 1} and {100/211} forms. Grains have faint oscillatory zonation or sector zoning. Convolute and disjointed boundaries between textures. Areas of homogeneously textured zircon appearing as transgressive (across all pre-existing textures) zircon patches and lobes.

Table 2

Summary age and hafnium isotope data from (meta)igneous samples.

Sample	Rock Type		Age (Ma)	2σ (Ma)	MSWD	n=	εHf(t) range	Inheritance (Age in Ma)
BU1	Monzogranite	^{206}Pb/^{238}U	839	5	0.55	22	+6.59 to + 9.54	
BU2 + BU6	Syenogranite	^{207}Pb/^{206}Pb	775	17	0.41	11	+7.95 to −31.12	
OU1	Coarse-grained syenogranite	^{207}Pb/^{206}Pb	661	27	0.79	6	−0.58 to −4.96	
OU2	Coarse-grained syenogranite	^{207}Pb/^{206}Pb	653	20	0.64	11	+ 2.04 and −4.47	964
OU3	Orthogneiss	^{207}Pb/^{206}Pb	1030	18	0.78	12	+8.72 and + 6.01	2753, 1967
CM1	Monzogranite	^{207}Pb/^{206}Pb	594	22	0.53	9	−4.69 and −21.32	1011
CM2	Syenogranite	^{207}Pb/^{206}Pb	597	23	0.79	11		
MK1	Mylonitised granite	^{206}Pb/^{238}U	571	4	1.7	34	−22.94 and −20.11	622
MK2 + MK3	Monzogranite	^{206}Pb/^{238}U	556	5	1.6	21	−19.42 and −22.02	

Table 3

Summary age and hafnium isotope data from metasedimetnary/volcanic samples (Ages in Ma).

Sample	Rock type	Age Peaks	YSG	2σ	YSP	2σ	MSWD
BU3	Meta-volcaniclastic	1837, 973	679	16	973	14	0.34
BU4 + BU5	Paragneiss	969, 738	633	20	945	13	1.2
OU4	Schist	1010, 690, 604	602	14	609	24	1.8
OU5	Muscovite schist	2648, 1970, 1082	967	27	987	10	0.69
CM3	Garnet-bearing psammitic schist	619, 696, 797, 940	584	15	689	27	1.7

YSG = youngest single grain, YSP = youngest single population